

# Draft Analysis Note

Austin Baty,<sup>1</sup> Zhenyu Chen,<sup>2</sup> Wei Li,<sup>3</sup> Stefan Schmitt,<sup>4</sup> Chuan Sun,<sup>5</sup> and Zhoudunming Tu<sup>6</sup>

<sup>1</sup>1

<sup>2</sup>2

<sup>3</sup>3

<sup>4</sup>4

<sup>5</sup>5

<sup>6</sup>6

Abstract

PACS numbers: To be done.

## I. INTRODUCTION

This paper presents the measurements of the two-particle angular correlations of charged particles emitted in ep collisions with 27.6 GeV e beam and 920 GeV proton beams. Multi-particle correlations in high-energy collisions provide valuable information for characterizing Quantum Chromodynamics (QCD) and have been studied previously for a broad range of collision energies and colliding systems. In high multiplicity proton-proton (pp), proton-nucleus (pA), and nucleus-nucleus (AA) collisions such measurements can elucidate modifications of the underlying mechanism of particle production and possible collective effects due to the high particle densities reached in these collisions.

Studies of two-particle angular correlations are typically performed using two-dimensional  $\Delta\eta - \Delta\phi$  correlation functions, where  $\Delta\eta$  is the difference in pseudorapidity  $\eta = -\ln(\tan(\theta/2))$  and  $\Delta\phi$  is the difference in azimuthal angle  $\phi$  between the two particles. The polar angle  $\theta$  is determined relative to the clockwise circulating beam.

Of particular interest in studies of possible novel collective effects is the long-range (large  $|\Delta\eta|$ ) structure of two-particle correlation functions, which can be understood as a consequence of the hydrodynamic flow of the produced strongly interacting medium. In hydrodynamic models, the detailed azimuthal structure of particle emission reflects the medium-response to fluctuations in the initial collision geometry and allows the determination of fundamental transport properties of the medium.

Measurements in pp collisions at 7 TeV have also revealed the emergence of long-range, near-side correlations in a selection of collisions with very high final state particle multiplicity. With the interactions of vector-meson and proton in ep collisions regarded as a sum of simultaneous QCD processes similar to pp collisions, it is natural to search for collectivity in ep resolved photoproduction processes, where a similar range of final state multiplicities can be explored. As the Deep-inelastic scattering (DIS) results show scatterings not contributing to collective flow in ep collisions, the long-range correlation structure in ep collisions with resolved photoproduction selections can provide valuable information for the origin of the possible collective effects in ep collisions.

In this letter, the two-particle correlation functions in ep collisions with DIS and photoproduction selections are shown and harmonics coefficients are also extracted for quantitative analysis.

+ MC explanations/ + yield measurements/ (to be done.)

## II. EVENT AND TRACK SELECTIONS

### A. Trigger and event selections

The ep collision events mainly consist of two regimes: the deep inelastic scattering(DIS) and photoproduction process, which can be distinguished by the  $Q^2$ , the exchanged photon virtuality defined by the four-momentum difference  $Q^2 = -(k - k')^2$ , where the  $k$  and  $k'$  represent the four-momentum of the incoming and outgoing electron, respectively. For the photoproduction process, the virtuality is quasi-real( $Q^2 \approx 0$ ), and for the DIS process the photon virtuality used in analysis is  $5 < Q^2 < 100$  GeV. A clear selection of events is essential for the two processes.

According to the Bjorken scalling description, the kinematic process in DIS can be characterized by a set of two of the three variables  $x$ ,  $y$  and  $Q^2$  in a fixed centre-of-mass energy  $\sqrt{s}$ . At Hera there are three reconstruction methods referring to different kinematic regions: electron method(using the scattered lepton), the  $\Sigma$  method(using the hadronic final state) and  $e\Sigma$  method(using a combination of both). Due to the effect of the initial state QED radiation and the poor resolution of the calorimeter, only the  $e\Sigma$  method can be used reasonably in this analysis. The kinematic variables are defined as mixture of the electron method and the  $\Sigma$  method.

In the electron method, the kinematic variables are calculated using the information of the scattered lepton, its energy  $E'_e$  and polar angle  $\theta_e$ , and  $E_e$  is the electron beam energy:

$$y_e = 1 - \frac{E'_e}{E_e} \sin^2 \frac{\theta_e}{2}, \quad Q_e^2 = 4E_e E'_e \cos^2 \frac{\theta_e}{2}, \quad x_e = \frac{Q_e^2}{sy_e} \quad (1)$$

In the  $\Sigma$  method, energy and momentum conservation requires that  $\Sigma_i(E_i - p_{z,i})$ , where  $i$  runs over all final state particles including the scattered electron, is equal to the two times the incident electron energy,  $2E_e$ .  $E - P_z = \Sigma_i(E_i - p_{z,i}) = \Sigma + E'(1 - \cos\theta_e) = 2E_e$ . So the  $(E - P_z)/2$  can be used to redefine the electron beam energy. The variables defined in this method are as follows, where the  $\Sigma$  means the sum of scalar quantities  $E_i - p_{z,i}$  of each particle in hadronic final state:

$$y_\Sigma = \frac{\Sigma}{E - P_z}, \quad Q_\Sigma^2 = \frac{E_e'^2 \sin^2(\theta_e)}{1 - y_\Sigma}, \quad x_\Sigma = \frac{Q_\Sigma^2}{sy_\Sigma} \quad (2)$$

In the  $e\Sigma$  method, the variables are the mixture of the two former methods:

$$Q_{e\Sigma}^2 = Q_e^2, \quad x_{e\Sigma} = x_\Sigma = \frac{Q_\Sigma^2}{sy_\Sigma}, \quad y_{e\Sigma} = \frac{Q_e^2}{sx_\Sigma} \quad (3)$$

The final state particles can be better studied with a boost to the hadronic centre-of-mass frame[1], where the virtual photon and proton can be colinear and  $\vec{p} + \vec{q} = 0$  ( $\vec{p}$  and  $\vec{q}$  are the momentum of the incoming proton and photon, respectively). This homogeneity in the rest frame can give convenience to the flow study because there is no bias introduced in momentum space. The variables are labeled as  $p_T^{lab}, \eta^{lab}, \phi^{lab}$  in lab frame and are labeled as  $p_T^{HCM}, \eta^{HCM}, \phi^{HCM}$  in HCM frame. In the HCM frame all hadronic final state particles which have  $p_z > 0$  are said to belong to the current hemisphere, and all particles with  $p_z < 0$  are assigned to the target or proton remnant hemisphere, which is shown in FIG. 1. The forward direction, the direction of the incoming proton, is pointing to negative  $\eta^{HCM}$ .

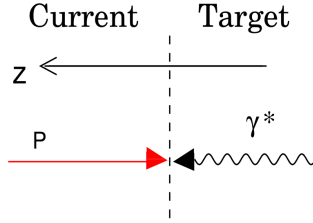


FIG. 1: The hadronic centre-of-mass system.

The Lorentz boost can be constructed by the four-vector of the virtual photon, which can be calculated using the kinematic variables mentioned above,  $Q^2$ ,  $y$  and the azimuthal angle of the scattered electron. The calculated variables, energy  $E_e^{reco}$ , polar angle  $\theta_e^{reco}$ , and the azimuthal angle  $\phi_e^{reco}$  of the scattered electron are as follows:

$$E_e^{reco} = \frac{Q_{e\Sigma}^2}{4E_e} + E_e(1 - ye\Sigma), \quad \theta_e^{reco} = \arccos \frac{1 - b}{1 + b} \quad (4)$$

where

$$b = 4E_e^2 \frac{1 - ye\Sigma}{Q_{e\Sigma}^2}, \quad \phi_e^{reco} = \phi_e \quad (5)$$

The azimuthal angle  $\phi_e^{reco}$  is used to rotate the HCM frame x-axis to the direction of the  $p_x$  of the scattered electron.

### 1. DIS data

The DIS data sample used in this analysis was taken in H1 detector at Hera during 2006-2007. During this period, the Hera accelerator collided 27.6 GeV  $e^\pm$  beams with 920 GeV proton beams, which yield a nominal centre-of-mass energy of 319 GeV. The measurement of the charged particle transverse momentum spectra is based on a selection of neutral current (NC) DIS events, which are defined through the scattered electron. The processes where photon/ $Z^0$  bosons are exchanged are called neutral current (NC) processes, whereas the exchange of a  $W^\pm$  is called a charged current (CC) process.

DIS events were recorded using triggers based on electromagnetic energy deposits in the SpaCal calorimeter. The trigger efficiency is determined using the independently triggered data. For DIS events the trigger inefficiency is negligible in the kinematic region of the analysis. The scattered lepton, defined by the most energetic SpaCal cluster, is required to have an energy  $E_e$  larger than 12 GeV. The kinematic phase space is defined by  $5 < Q^2 < 100 \text{ GeV}^2$  and  $0.0375 < y < 0.6$ , corresponding to the geometric acceptance of the SpaCal. The upper cut on  $y$  reduces background from the photoproduction. In addition,  $x$  is required to be in the range of  $0.0001 < x < 0.01$ .

Additional selections are made to reduce QED radiation effects and to suppress background events. The  $z$  coordinate of the event vertex is required to be within 35 cm of the nominal interaction point. Events with high energy initial state photon radiation are rejected by requiring  $35 < \sum_i (E_i - p_{z,i}) < 75 \text{ GeV}$ . Here, the sum extends over all hadronic final state particles and the scattered electron. Besides, considering the implementing of the 2PC method in flow analysis, the number of selected tracks in each events are required to be more than 2.

The distributions of the variables in DIS are shown in the following FIG.2.

### 2. photoproduction data

In pQCD, at leading order, two classes of processes contribute to the photoproduction events where the photon emitted by the positrons interacting with the proton: the direct-photon process and the resolved-photon process, which are shown in FIG. 3. In the direct process, the photon enters the hard process directly. In resolved process the photon fluctu-

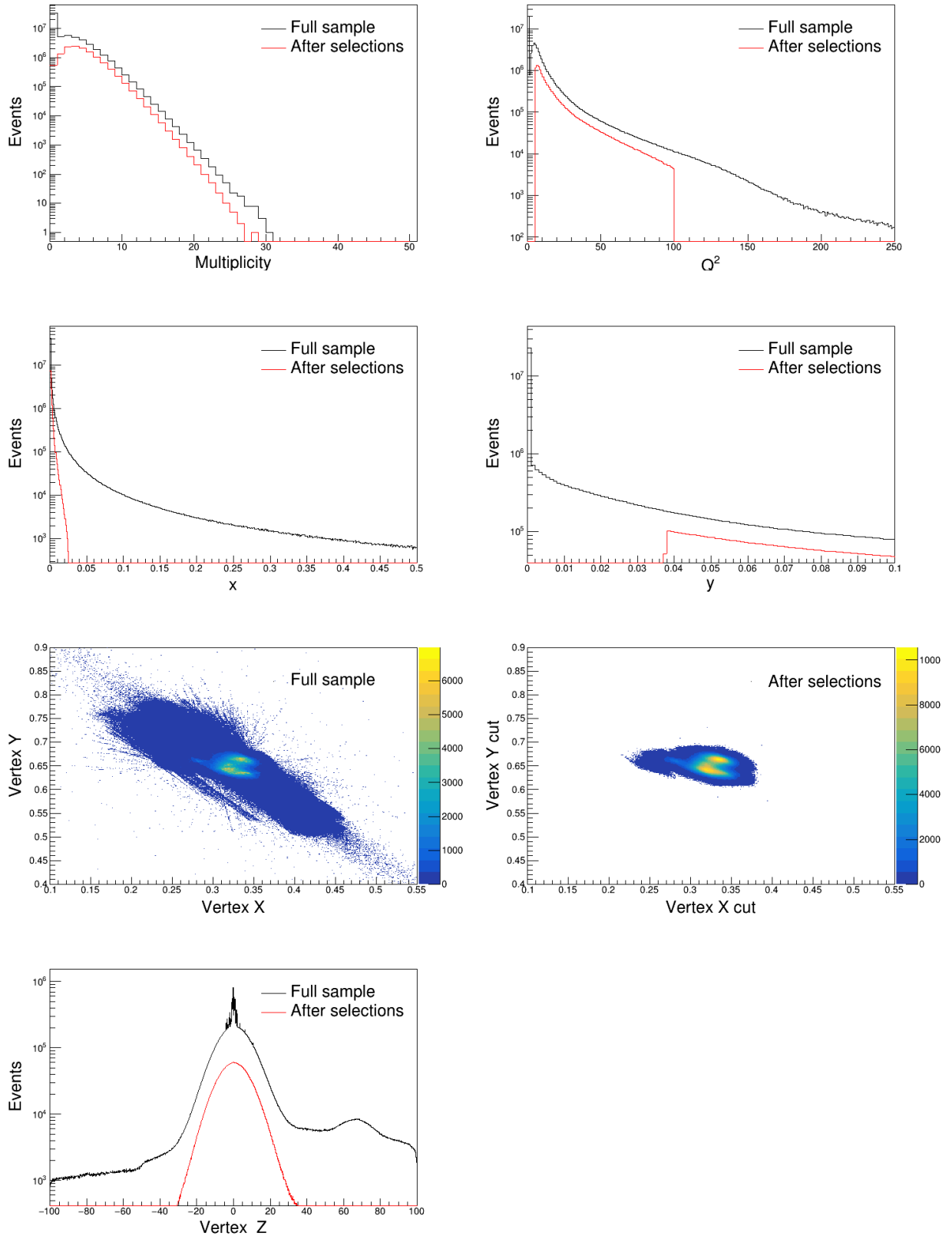


FIG. 2: Distributions in DIS process data. The black line and red lines represent the situations without and within event selections. The multiplicity is defined by track selections on  $0.3 < p_T^{lab} < 3.0$ ,  $-1.6 < \eta^{lab} < 1.6$ .

ates into a hadronic state and takes part in the hard process as a cluster of partons. The direct photoproduction process which dominates in hard scattering has fewer multiplicity compared with that in resolved process which is abundant in quasi-real region. The resolved process, suppressed in higher  $Q^2$ , can be gathered in high multiplicity within our following data selections.

The vector-meson and proton collision in resolved photoproduction process is the focus of our flow analysis for ep collisions. The near-side ridge structure, as well as a signal of collectivity, is seen in high multiplicity 2PC functions in pp collisions. While in low multiplicity pp collisions, clear evidence of collectivity has not been observed. As the resolved process in ep collisions can be regarded as hadronic collisions, which is similar to pp collisions, the search for collectivity in high multiplicity resolved photoproduction events could therefore provide insights on the origin of collectivity in small colliding systems.

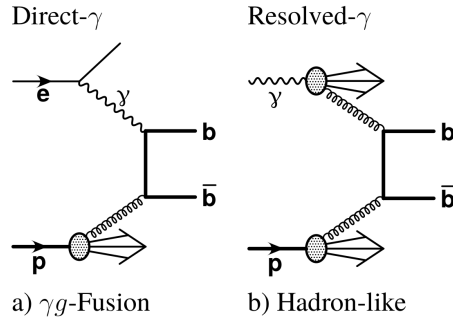


FIG. 3: Direct and resolved photoproduction processes.

The photoproduction data is triggered by the signal of scattered electrons in electron tagger. Additional selections are applied on tagged position  $x_{position}$ , tagged electron energy  $E_e^{tagged}$ , and tagged photon energy  $E_\gamma^{tagged}$ . They restrict that  $x_{position} + 0.4E_e^{tagged} > 0$  and  $-3.0 < x_{position} < 3.0$ .  $E_e^{tagged} + E_\gamma^{tagged} < 20$  can help determine the  $Q^2$  between the photon and proton by the upper limit on the sum of the diffracted photon energies and the scattered electron.

To ensure the presence of backward-going particles, a selection of the minimum value of  $\eta < 0$  is required. The  $z$  coordinate of the event vertex is required to be within 30 cm of the nominal interaction point.

The distributions of the variables in photoproduction are shown in the following FIG.4.

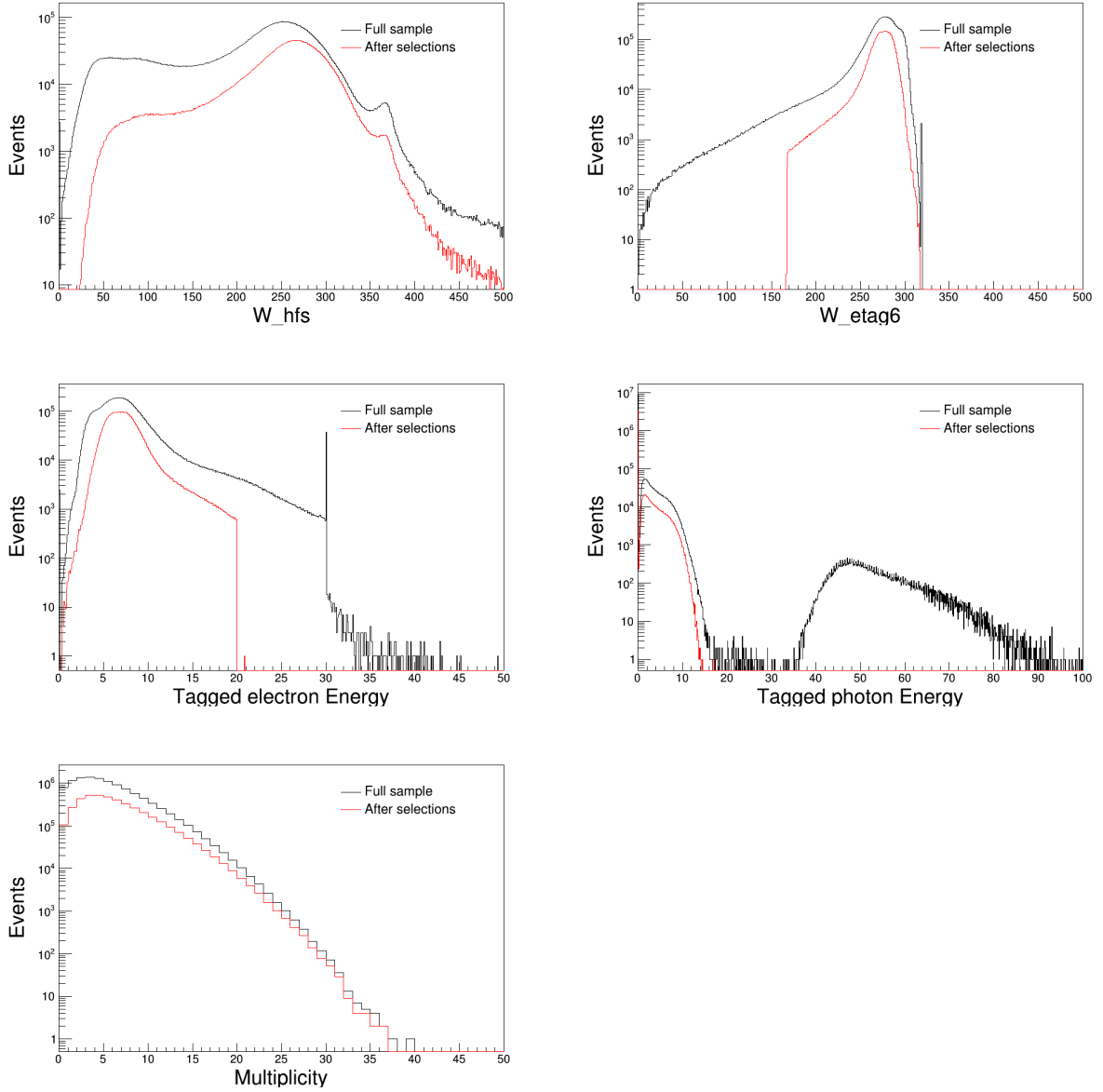


FIG. 4: The distributions of photoproduction events in ep collisions. The black and red lines represent the situations without and within event selections. The  $W_{hfs}$  and  $W_{etag6}$  are the calculated centre-of-mass energy of the photon and proton, from the hadronic final state information and tagged electron energies respectively. The multiplicity is defined by track selections on  $0.3 < p_T^{lab} < 3.0$ ,  $-1.6 < \eta^{lab} < 1.6$ , which is equal to the DIS multiplicity definitions.



## B. Track selections

There are several types of track candidates available in the H1 reconstruction software: the track measured only in central devices (CJC - the central drift chamber, CST - a Central Silicon Track detector, z-chambers) - central tracks (C); the tracks measured only with FTD - forward tracks (F); and combined tracks (K), measured in central and forward trackers. Furthermore, tracks can be reconstructed assuming their origin at the primary vertex(1) or at the secondary vertex(2).

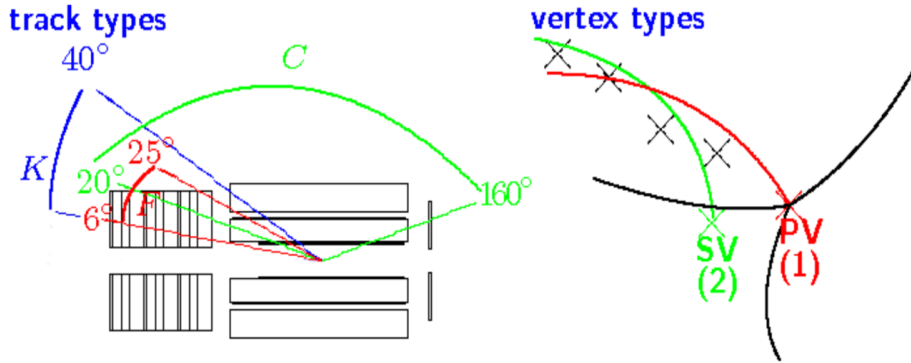


FIG. 5: Different types of track and vertex in H1 reconstruction procedure.

Since a track might be assigned to more than one type, double counting is possible. This issue can be resolved by the following procedure. First, only "good" tracks are selected, which pass the default tracks cuts, so-called "Lee West track selection". The cuts are different for each track type and are listed in FIG.6. In the second step the preference for one track type over the others for a selected track is taken, thus the double counting is removed. The choice of the best track type is discussed below.

All reconstructed data after the fourth level trigger but before the physics analysis selection are stored in the lowest level of the storage system - ODS (Object Data Store). The selected data are stored in the next level of the storage system ( $\mu$ ODS - Micro Object Data Store), which is smaller in size than the ODS and essentially stores the final state information allowing a substantially faster event selection.

On  $\mu$ ODS the following strategy for the selection of the best track hypothesis is applied in FIG.6.

Central tracks	
$p_T > 0.07 \text{ GeV}$	Track transverse momentum
$ dca' \cdot \sin(\theta)  \leq 2 \text{ cm}$	$dca'$ - distance of closest approach of the track in the $r\varphi$ plane to the primary vertex
$R_{\text{start}} \leq 50 \text{ cm}$	Start point of first hit
$R_{\text{length}} \geq 10 \text{ cm for } \theta \leq 150^\circ$ $R_{\text{length}} \geq 5 \text{ cm for } \theta > 150^\circ$	Radial distance between first and last hits
$N_{\text{CJC hits}} \geq 0$	Number of hits in <b>CJC</b>
Combined tracks	
$p_T > 0.12 \text{ GeV}$	Track transverse momentum
$p > 0.5 \text{ GeV}$	Track momentum
$10^\circ < \theta < 30^\circ$	Track polar angle
$ dca'  \leq 5 \text{ cm}$	Distance of closest approach of the track in the $r\varphi$ plane to the primary vertex
$R_{\text{start}} \leq 50 \text{ cm}$	Start point of first hit
$N_{\text{CJC hits}} \geq 0$	Number of hits in <b>CJC</b>
$\frac{\Delta p}{p} < 99999.9$	Track momentum resolution
Fit $\chi^2 < 50$	$\chi^2$ of vertex fit
$\chi_{c-f}^2 < 50$	$\chi^2$ of link between central and forward tracks
Forward tracks	
$p_T > 0.12 \text{ GeV}$	Track transverse momentum
$p > 0.5 \text{ GeV}$	Track momentum
$6^\circ < \theta < 25^\circ$	Track polar angle
$R_{\text{start}} \leq 25 \text{ cm}$	Start point of first hit
$z_{\text{length}} \geq 10 \text{ cm}$	$z$ distance between first and last hits
$R_0 \leq 20 \text{ cm}$	Radial distance of the track from the beamline
$\frac{\Delta p}{p} < 99999.9$	Track momentum resolution
Fit $\chi^2 < 25$	$\chi^2$ of vertex fit
$\chi^2 < 10$	$\chi^2$ of track fit

FIG. 6: Cuts for "good" central, combined and forward tracks.

We only use the central and combined tracks due to the worse momentum resolution in forward direction. For this analysis, additional track selections as  $0.3 < p_T^{lab} < 3.0 \text{ GeV}$ ,  $-1.6 < \eta^{lab} < 1.6$  are included for DIS track selections, listed in FIG.7. In photoproduction data,  $0.3 < p_T^{lab} < 3.0 \text{ GeV}$ ,  $-2.0 < \eta^{lab} < 2.0$  are added.

The distributions of the tracks information in photoproduction selections are listed in FIG.8:

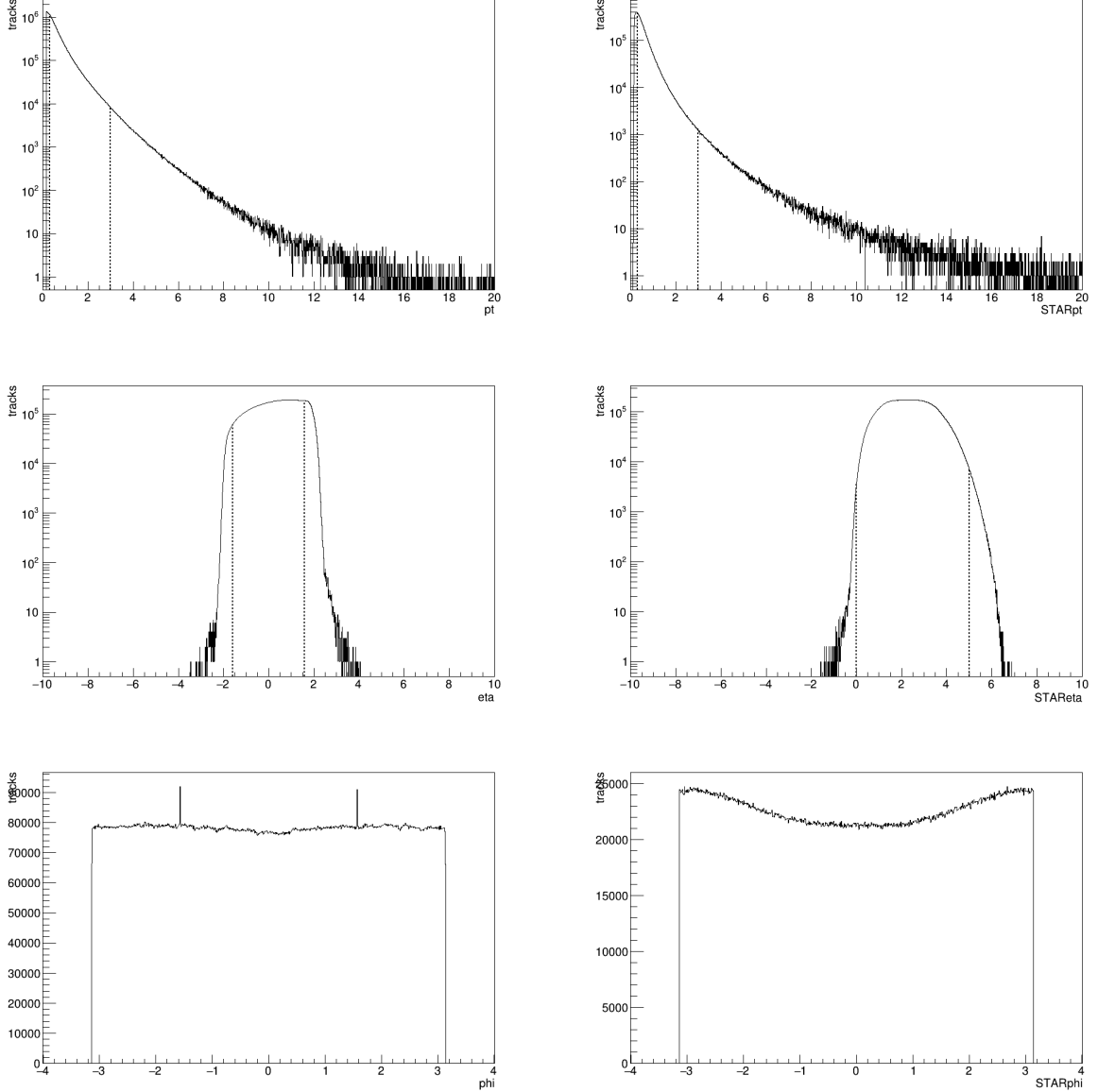


FIG. 7: Distributions of the DIS events track level information, including that in lab frame and in HCM frame. Dash lines indicate track selection cuts.

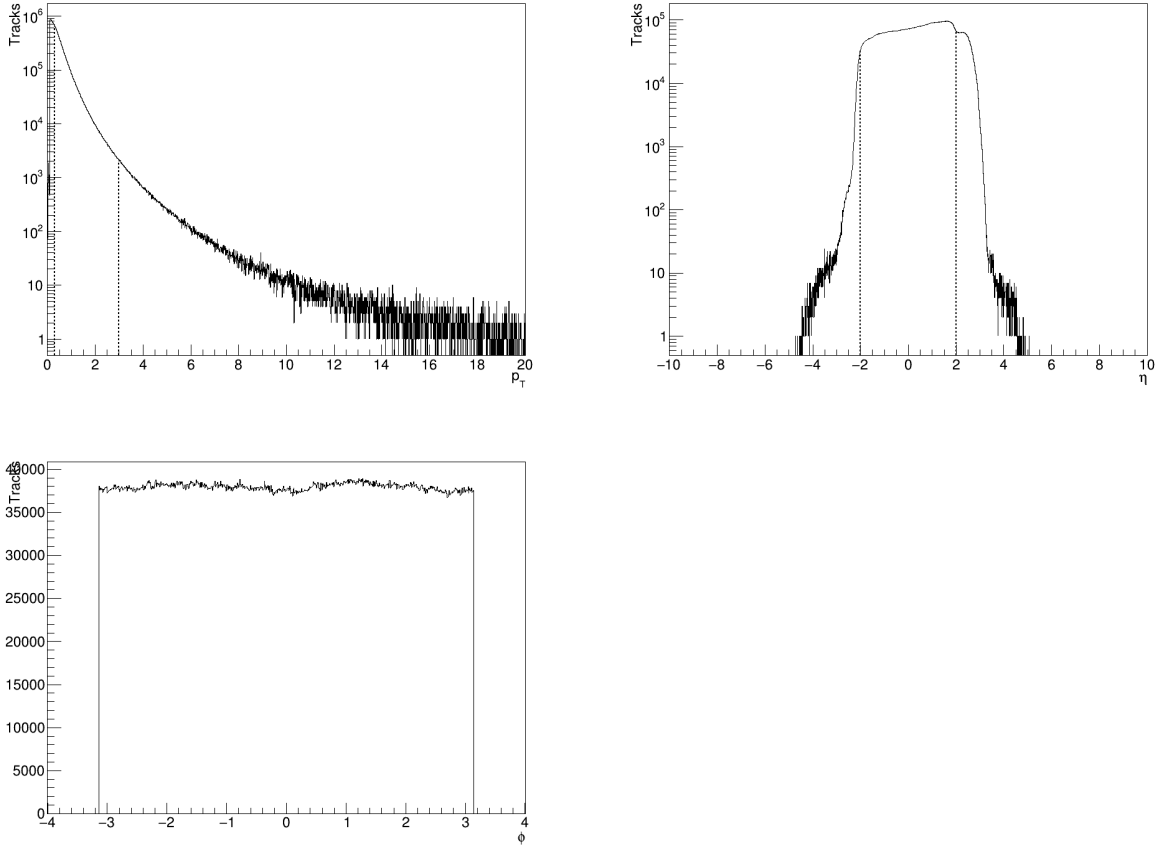


FIG. 8: Distributions of the photoproduction events track level information.

### III. ANALYSIS TECHNIQUE

The raw event-by-event multiplicity distributions in H1 ep collisions DIS data(left) and photoproduction data(right) are shown below and the analysis begins with the divisions on multiplicities. The multiplicity distributions defined in this analysis are counted within the following lab-frame kinematic selections:  $0.3 < p_T^{lab} < 3.0 GeV$ ,  $-1.6 < \eta^{lab} < 1.6$ . There are 8 track multiplicity bins after the divisions, including:  $[2, 4]$ ,  $[4, 6]$ ,  $[6, 8]$ ,  $[8, 10]$ ,  $[10, 12]$ ,  $[12, 15]$ ,  $[15, 20]$ ,  $[20, 999]$ . The fractions of the overall distribution are shown in FIG.9.

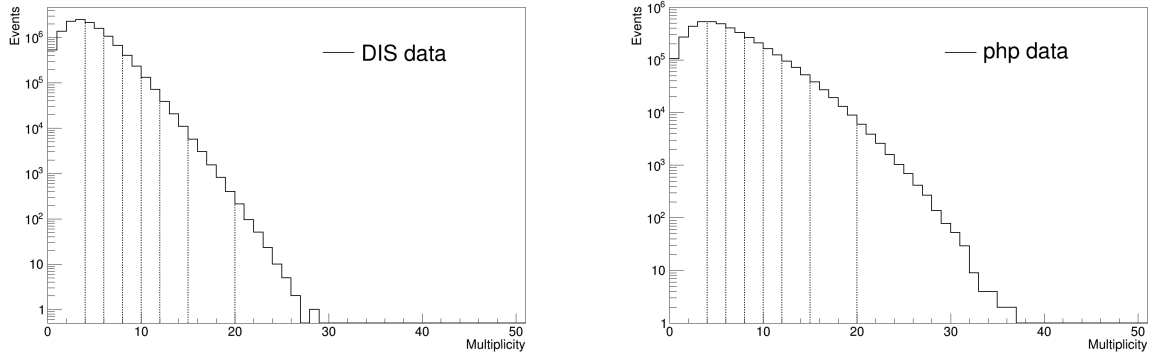


FIG. 9: The distributions of the multiplicity in DIS and photoproduction selections. The multiplicity is defined as the number of tracks within  $0.3 < p_T < 3.0$  GeV,  $-1.6 < \eta < 1.6$ .

Multiplicity bin( $N_{trk}^{offline}$ )	Fraction(%)
Minimum Bias	100.00
$2 \leq N_{trk}^{offline} < 4$	22.89
$4 \leq N_{trk}^{offline} < 6$	24.00
$6 \leq N_{trk}^{offline} < 8$	17.54
$8 \leq N_{trk}^{offline} < 10$	11.22
$10 \leq N_{trk}^{offline} < 12$	6.81
$12 \leq N_{trk}^{offline} < 15$	5.20
$15 \leq N_{trk}^{offline} < 20$	2.52
$20 \leq N_{trk}^{offline} < 999$	0.40

### A. Two-particle Correaltion Method(2PC)

The Two-particle correlation(2PC) method is used in this analysis, and the procedure is similar to the ones in Ref.XX. Charged particles in each event are defined as the trigger particles, and the number of them is denoted as  $N_{trig}$ . When pairing trigger particles, the associate particles are also kept in the same multiplicity range and within same track selections in HCM frame:  $0.3 < p_T^{HCM} < 3.0 GeV$ ,  $0.0 < \eta^{HCM} < 5.0$ . The 2PC functions are filled by the difference  $\Delta\eta, \Delta\phi$  in HCM frame on the average of  $N_{trig}$ . So in the same

event, the differential per-trigger-particle yield distributions can be given by:

$$\frac{1}{N_{trig}} \frac{d^2 N^{pair}}{d\Delta\eta d\Delta\phi} = B(0,0) \times \frac{S(\Delta\eta, \Delta\phi)}{B(\Delta\eta, \Delta\phi)} \quad (6)$$

where the S, B are called the signal and background distributions, respectively. The signal distribution, is per-trigger-particle yield of same-event correlated pairs,

$$S(\Delta\eta, \Delta\phi) = \frac{1}{N_{trig}} \frac{d^2 N^{same}}{d\Delta\eta d\Delta\phi} \quad (7)$$

The background distributions is found using a mixed event technique, wherein trigger particles from one event are combined with all of the associated particles from a different event within  $|Z_{VTX}| < 2cm$  along the beam direction. In this analysis, associated particles from 5 randomly chosen evnets are used. The result is given by,

$$B(\Delta\eta, \Delta\phi) = \frac{1}{N_{trig}} \frac{d^2 N^{mix}}{d\Delta\eta d\Delta\phi} \quad (8)$$

The background distribution is dominated by the pair-acceptance effects under random combinations. The value of the  $B(0,0)$  at  $(\Delta\eta, \Delta\phi) = (0,0)$  is a normalization factor, with a bin width of 0.1 in  $\Delta\eta$  and  $\frac{2\pi}{33}$  in  $\Delta\phi$ , truly referring the full pair-acceptance when two correlated particles in one pair going in approximately same direction. After the pair-acceptance correction, the final 2PC distributions can also get corrected. Considering the statistical precision, the true value of  $\Delta\phi$  and the absolute value of  $\Delta\eta$  are used to fill two quadrant of the 2PC histograms, with the other two quadrants filled by reflections. Therefore, the resulting distributions are symmetric in  $\Delta\eta$  direction.

A instance of signal and background pair distributions are shown for  $0.3 < p_T^{HCM} < 3.0 GeV$  in ep DIS collisions data for multiplicity bin [15, 20]. The triangle shape in  $\Delta\eta$  is due to the limited acceptance in  $\Delta\eta$  direction as the phase space obtaining two particles in one pair can reach most in the same eta direction and become smaller when  $\Delta\eta$  aggrandizes. By taking a ratio between the signal and background distributions, all dependence on  $\Delta\eta$  and  $\Delta\phi$  from detector acceptance can be canceled. The corresponding 2PC functions in multiplicity bin [15, 20] is shown in FIG.10.

To quantify the correlation function structure, the 2-D distribution function can be reduced to 1-D distribution function on  $\Delta\phi$  by averaging over a specified  $\Delta\eta$  region. The zero-yield-at-minimum(ZYAM) procedure is usually used to estimate the correlated portion of the associated yield. In this procedure, the 1-D distribution function is fitted by a second-order polynomial in a  $\Delta\phi$  region [1, 2.5], and the minimum value of the polynomial,  $C_{ZYAM}$ ,

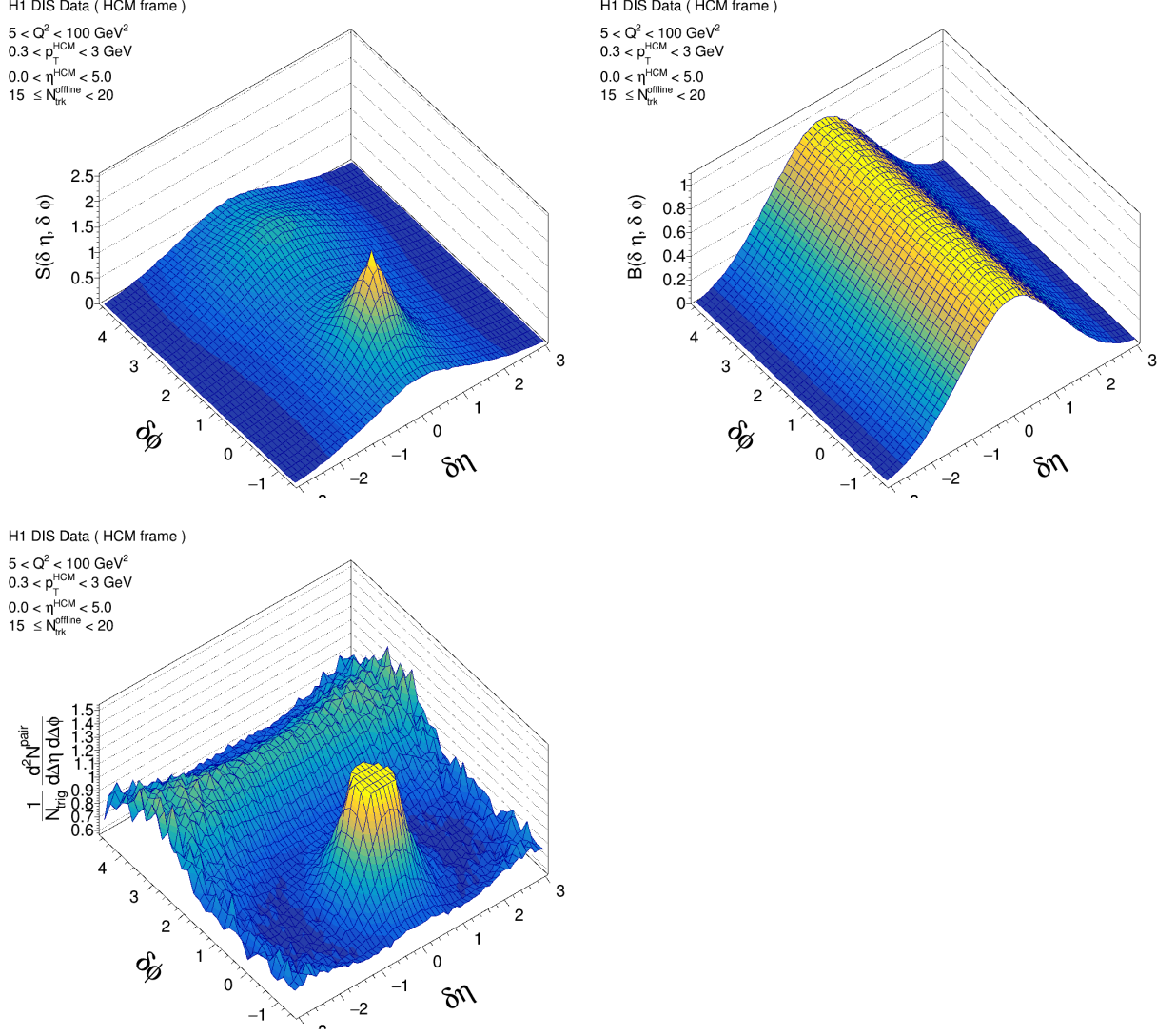


FIG. 10: Signal, mix-event background and the final functions of the 2-D 2PC for the  $0.3 < p_T^{HCM} < 3.0 \text{ GeV}$ ,  $0.0 < \eta^{HCM} < 5.0$  ep DIS data with  $15 \leq N_{trk}^{offline} < 20$ . No near-side ridge structure in the final functions in all multiplicities.

is then subtracted from the original 1-D distribution function along  $\Delta\phi$ . Then the minimum of the 1-D distribution function is shifted and has no associate yield. After the procedure, these 1-D distributions along  $\Delta\eta$  direction, are projections integrated on four different  $\Delta\eta$  bins:  $[0, 1]$ ,  $[1, 1.5]$ ,  $[1.5, 2]$ ,  $[2, 3]$ , and the FIG.11 shows the comparisons between  $\Delta\phi$  distributions in long-range  $\Delta\eta$  region.

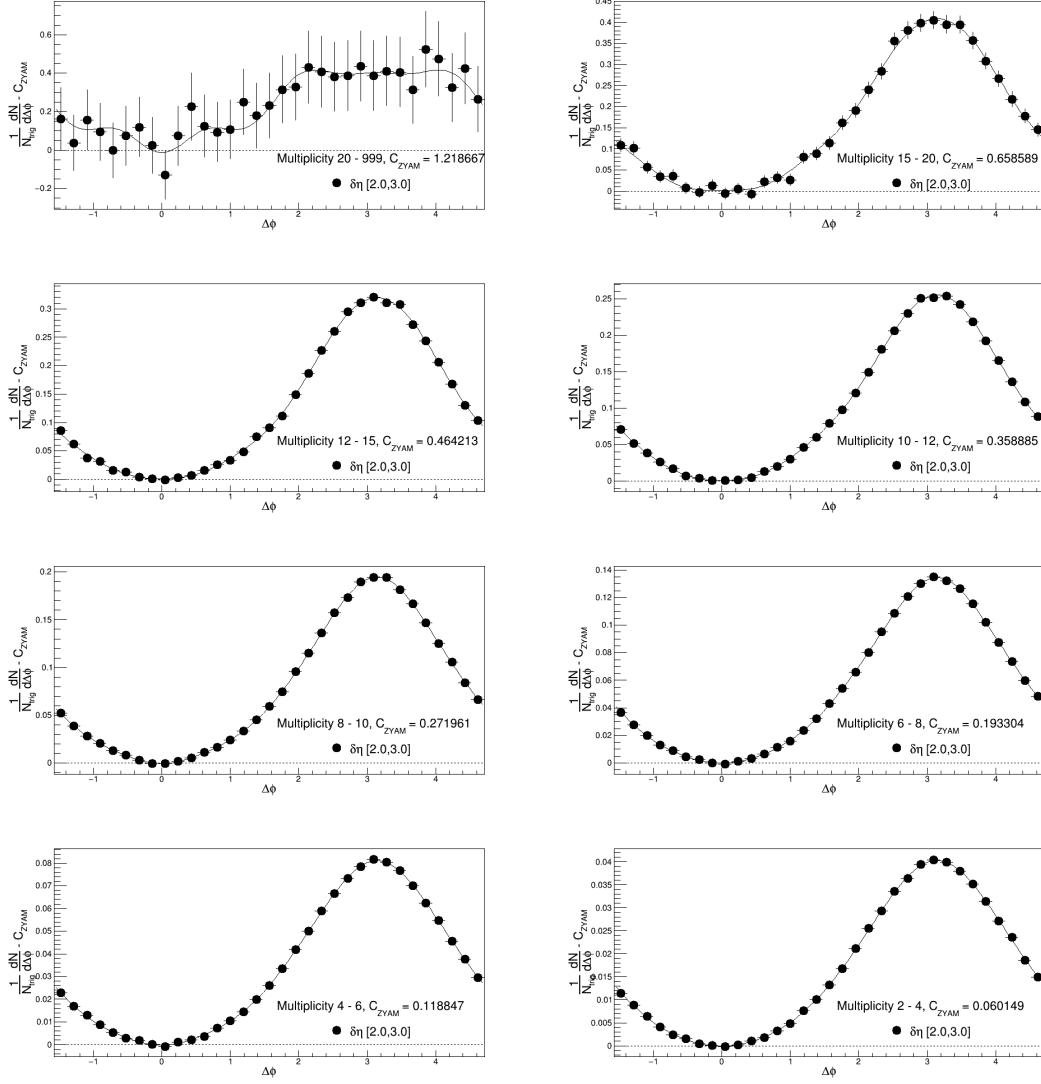


FIG. 11: After the zero-yield-at-minimum(ZYAM) procedure, long-range structure(corresponding to  $2.0 < \Delta\eta < 3.0$ ) in 2PC functions of DIS selections in all multiplicities are listed here.

## B. Azimuthal Anisotropy Harmonics from Two-Particle Correlations

The azimuthal anisotropy harmonics are determined from a Fourier decompositons of long-range two-particle correlation functions on  $\Delta\phi$  direction,

$$\frac{1}{N_{trig}} \frac{dN^{pair}}{d\Delta\phi} = \frac{N_{assoc}}{2\pi} \left( 1 + \sum_n 2V_{n\Delta} \cos(n\Delta\phi) \right) \quad (9)$$

as described in Ref.XX, where the  $V_{n\Delta}$  is the Fourier coefficients and  $N_{assoc}$  represents the total number of pairs per trigger particle. An  $\eta$  gap of  $[2, 3]$  is applied to remove short-



range correlations from jet fragmentation in ep DIS processes analysis, and an  $\eta$  gap of [3, 4] is applied in photoproduction analysis. The trigger and associate particles are all from the same  $p_T$  region [0.3, 3], so the elliptic and triangular anisotropic harmonics,  $v_2$  and  $v_3$  extracted as  $v_n = \sqrt{V_{n\Delta}}$  from the 2PC functions Fourier fitting coefficients are also in same  $p_T$  region.

### C. Non-flow removal procedure

Fourier coefficient  $V_{n,n}$  can be extracted from the 1-D 2PC functions along  $\Delta\phi$  direction. To separate the potential ridge and the non-flow distributions such as jets, non-flow removal methods have been developed, including peripheral subtraction procedure(proposed by ALICE) and template fit procedure(proposed by ATLAS). They both based on several assumptions, such as no long-range correlations in peripheral event(low-multiplicity event), and jet-induced correlation shapes are invariant in all multiplicities. In this analysis, two methods are both used and compared.

In the non-flow cut procedure, the modified peripheral 2PC functions can provide the information of jet yields.  $V_{n,n}$  extracted from the original 2PC functions, can be separated into the ridge and non-flow information according to the specific non-flow cut method, using the modified peripheral 2PCs functions.

#### 1. Peripheral subtraction method

By assuming that the jet-induced correlation shapes are invariant in multiplicity, the peripheral subtraction procedure is proposed by the ALICE by subtracting the results in the lowest multiplicity events, where the ridge signal is not present, from the high multiplicity events. Fourier coefficient  $V_{n,n}$ , extracted from high multiplicity events, can be subtracted by the  $V_{n,n}$  from the lowest multiplicity [2, 4] multiplied with a scale factor:

$$V_{n\Delta}^{sub} = V_{n\Delta} - V_{n\Delta}(2 \leq N_{trk}^{offline} < 4) \times \frac{N_{assoc}(2 \leq N_{trk}^{offline} < 4)}{N_{assoc}} \times \frac{Y_{jet}}{Y_{jet}(2 \leq N_{trk}^{offline} < 4)} \quad (10)$$

Where the  $Y_{jet}$  represents the near-side jet yield. The ratio,  $\frac{Y_{jet}}{Y_{jet}(2 \leq N_{trk}^{offline} < 4)}$ , is introduced to account for the enhanced jet correlations due to the selection of higher multiplicity bins;

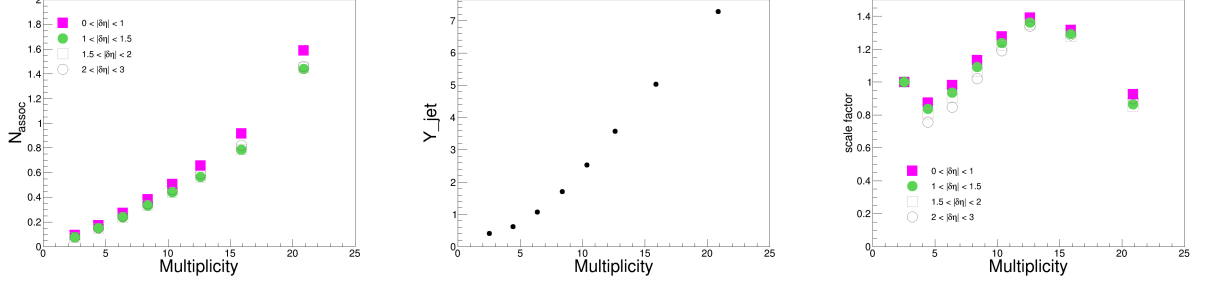


FIG. 12: Distributions of the  $N_{assoc}$ ,  $Y_{jet}$  and the whole scale factor versus multiplicity in  $0.3 < p_T^{HCM} < 3.0$  GeV,  $0.0 < \eta^{HCM} < 5.0$  ep DIS data. The scale factor variable is the value of  $\frac{N_{assoc}(2 \leq N_{trk}^{offline} < 4)}{N_{assoc}} \times \frac{Y_{jet}}{Y_{jet}(2 \leq N_{trk}^{offline} < 4)}$ .

the  $N_{assoc}$  represents the total pairs per trigger particle in a multiplicity bin, and the ratio  $\frac{N_{assoc}(2 \leq N_{trk}^{offline} < 4)}{N_{assoc}}$  considers the difference in the amount of pairs between multiplicities. The values of these parameters are shown in FIG.12. The plot of scale factor versus multiplicity shows that the  $[2, 4]$  multiplicity point doesn't follow the overall tendency, which indicates that it's perhaps not a good baseline for our non-flow procedure. The results with higher multiplicity as baseline are mentioned in Section V.C.

In DIS analysis, considering the need to keep same acceptance, in this peripheral subtraction procedure, the  $Y$  and  $N_{assoc}$  are calculated in the modified peripheral 2PCs with 2-D  $Q^2$  and  $y$  distributions weighting into the ones in the aimed multiplicity. In photoproduction analysis, the weighted quantity is the calculated collision energy using final state information.

## 2. Template fit method

In this procedure, the measured  $Y(\Delta\phi)$  distributions are assumed to result from a superposition of a peripheral  $Y(\Delta\phi)$  distribution,  $Y_{periph}(\Delta\phi)$ , scaled up by a multiplicative factor and a constant modulated by  $\sum \cos(n\Delta\phi)$  for  $n \geq 2$ . The resulting template fit function,

$$Y^{templ}(\Delta\phi) = Y^{ridge}(\Delta\phi) + FY^{periph}(\Delta\phi) \quad (11)$$

where

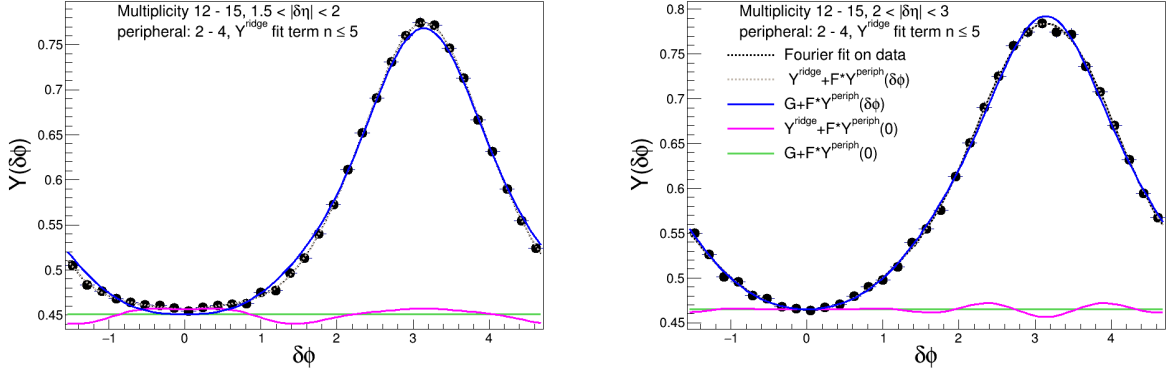


FIG. 13: The fitting on the  $Y_{ridge}(\Delta\phi)$  (purple-red line) of the  $0.3 < p_T^{HCM} < 3.0$  GeV,  $0.0 < \eta^{HCM} < 5.0$  ep DIS data includes harmonics  $n \leq 5$ . In multiplicity bin  $[2, 4]$ , the purple-red line is covered by the green one.

$$Y^{ridge}(\Delta\phi) = G \left( 1 + \sum_{n=2}^{\infty} 2v_{n,n} \cos(n\Delta\phi) \right) \quad (12)$$

has free parameters  $F$  and  $v_{n,n}$ . A  $v_{1,1}$  component is not included in  $Y_{periph}(\Delta\phi)$  as the presence of  $v_{1,1}$  in  $Y(\Delta\phi)$  is accounted by the  $Y_{periph}(\Delta\phi)$  term, as it represents the momentum conservation of decay processes which are included in the low multiplicity bin. The parameter  $F$  is the multiplicative factor by which the  $Y_{periph}(\Delta\phi)$  is scaled. The coefficient  $G$ , which represents the magnitude  $Y_{templ}(\Delta\phi)$  be equal of the combinatoric component of  $Y_{ridge}(\Delta\phi)$ , is fixed by requiring that the integral of  $Y_{templ}(\Delta\phi)$  equal to the integral of the measured  $Y(\Delta\phi)$ . In this analysis, when studying the multiplicity dependence of the long-range correlations, the  $[2, 4]$  multiplicity bin is defined as the peripheral one and provides the  $Y_{periph}(\Delta\phi)$  term. The distributions of the mentioned parameters are shown in FIG.13.

In this analysis, only the  $Y_{periph}(\Delta\phi)$  term comes from the modified peripheral 2PCs with weighted  $Q^2, y$  and  $p_T^{HCM}$ .

### 3. *MC studies on non-flow removal procedure*

Studies of the DIS processes using two-particle correlations have also been performed using ep MC generators: DJANGO and RAPGAP. The selections are similar to the ones in H1 data:  $5 < Q^2 < 100 \text{ GeV}^2$  and  $0.0375 < y < 0.6$  on event selections and  $0.3 < p_T^{HCM} < 3.0 \text{ GeV}$ ,  $0.0 < \eta^{HCM} < 5.0$  on track selections. The basic variables distributions on generator level are shown in FIG.14-15.

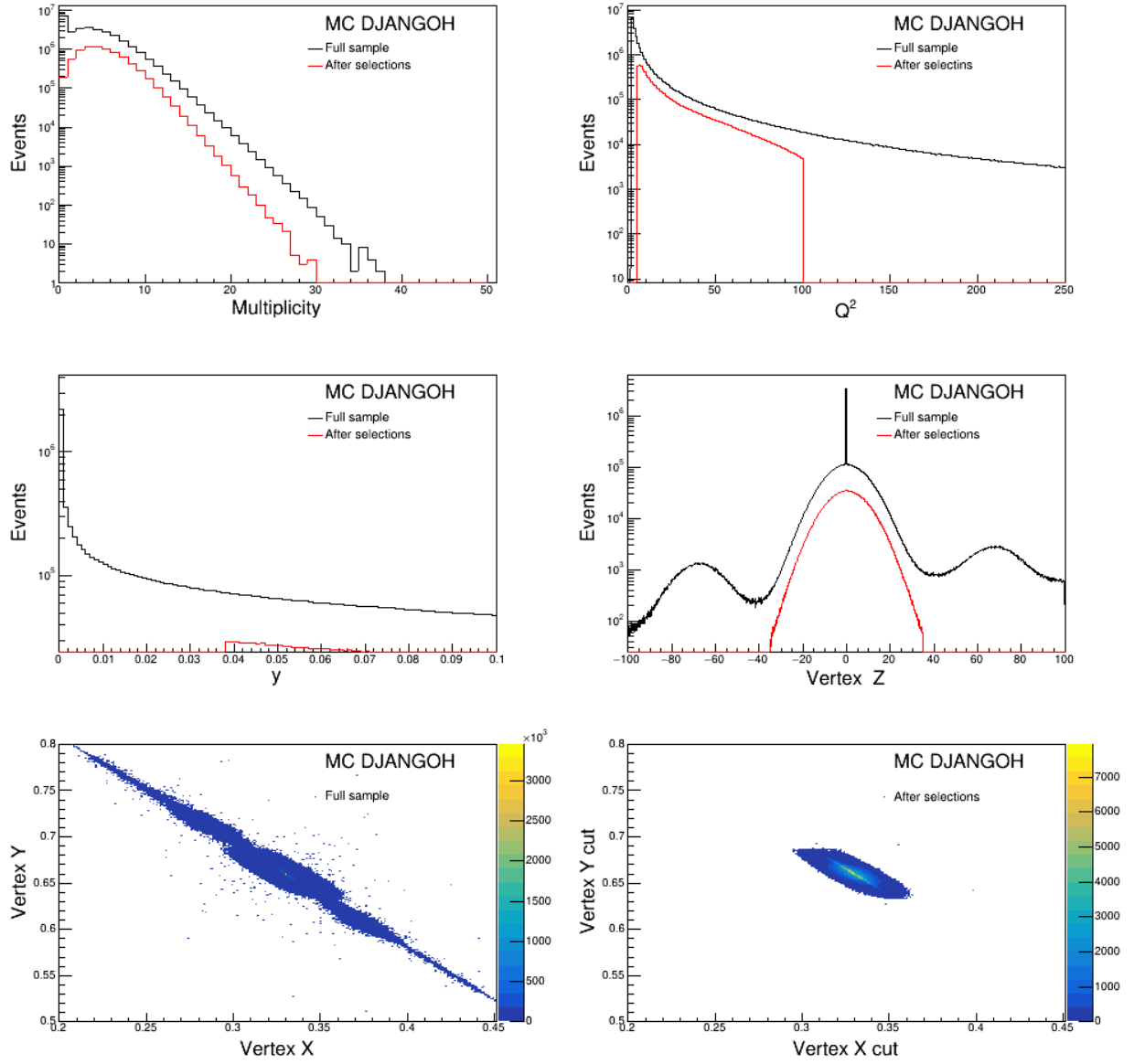


FIG. 14: Distributions of the event level information of ep DIS simulations in MC DJANGO. The mutliplicity is defined as same in H1 data,  $0.3 < p_T^{lab} < 3.0$ ,  $-1.6 < \eta^{lab} < 1.6$ .

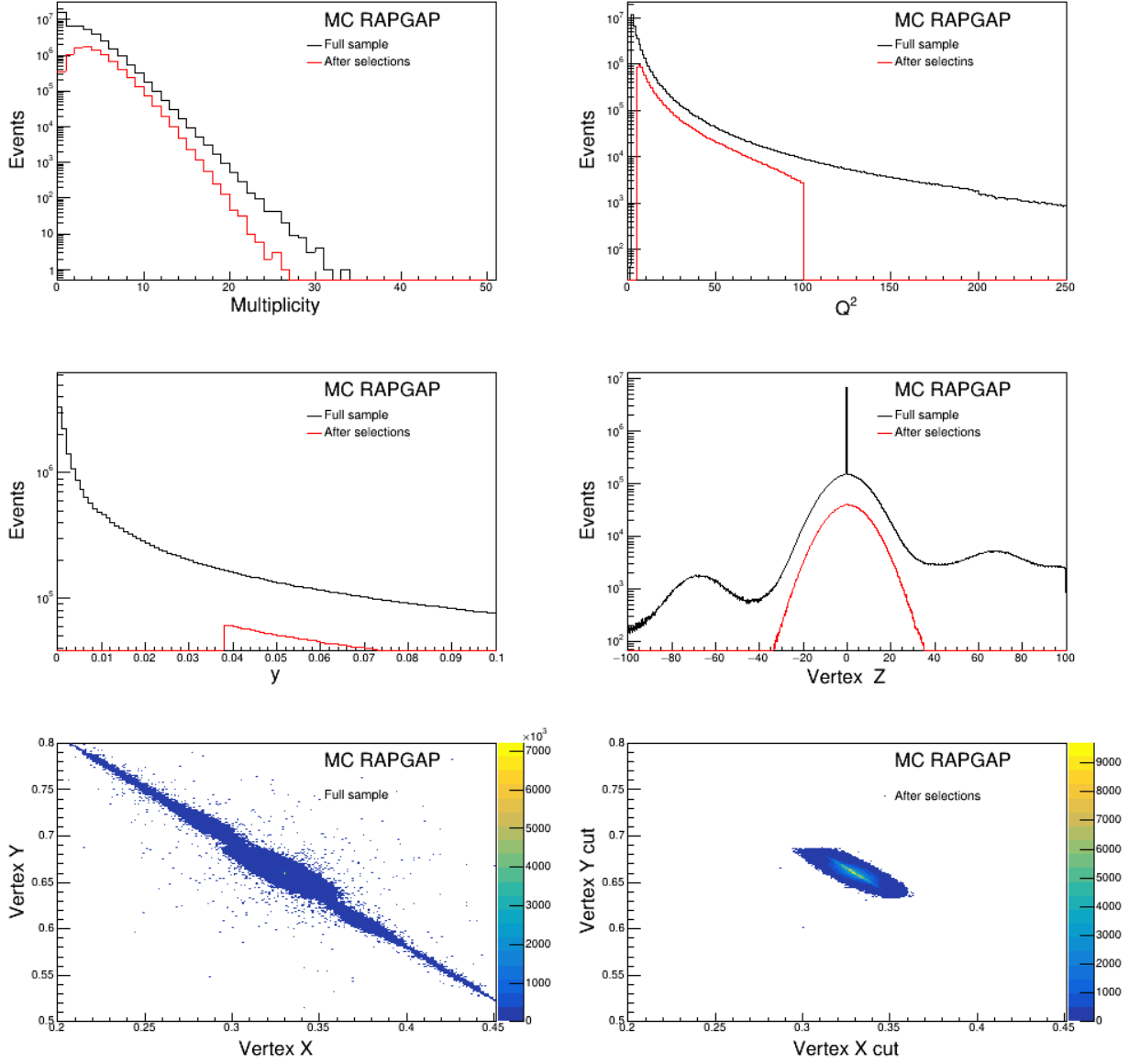
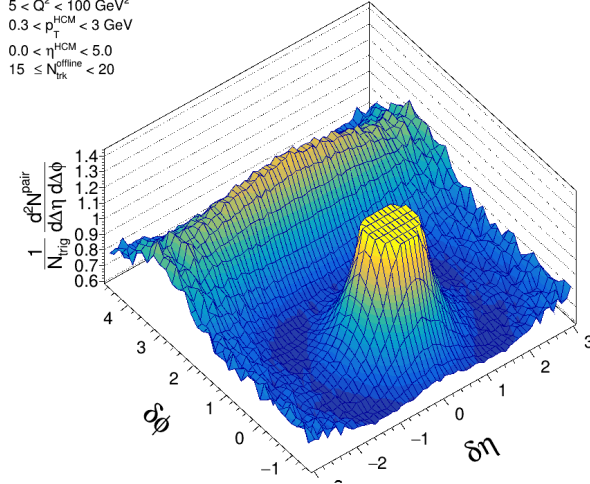


FIG. 15: Distributions of the event level information of ep DIS simulations in MC RAPGAP. The multiplicity is defined as same in H1 data,  $0.3 < p_T^{lab} < 3.0$ ,  $-1.6 < \eta^{lab} < 1.6$ .

The two-particle correlation functions in the multiplicity bins in MC DIS simulations are shown in FIG. 16, where no near-side ridge is seen. Both of the two models can give reasonable descriptions of data. As there is no collectivity behaviors in MC, the 2PCs after the non-flow removal procedure should get  $V_{n,n} \sim 0$ . Firstly the 1-D projections within ZYAM procedure on  $\Delta\phi$  direction are shown in FIG. 17.

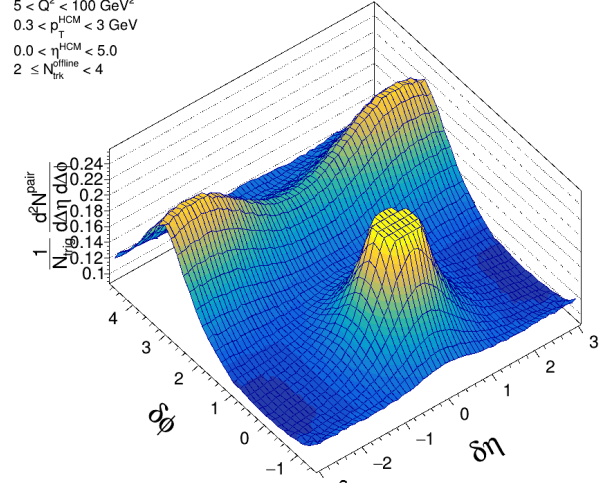
MC DJANGO DIS ( HCM frame )

$$\begin{aligned}
 &5 < Q^2 < 100 \text{ GeV}^2 \\
 &0.3 < p_T^{\text{HCM}} < 3 \text{ GeV} \\
 &0.0 < \eta^{\text{HCM}} < 5.0 \\
 &15 \leq N_{\text{trk}}^{\text{offline}} < 20
 \end{aligned}$$



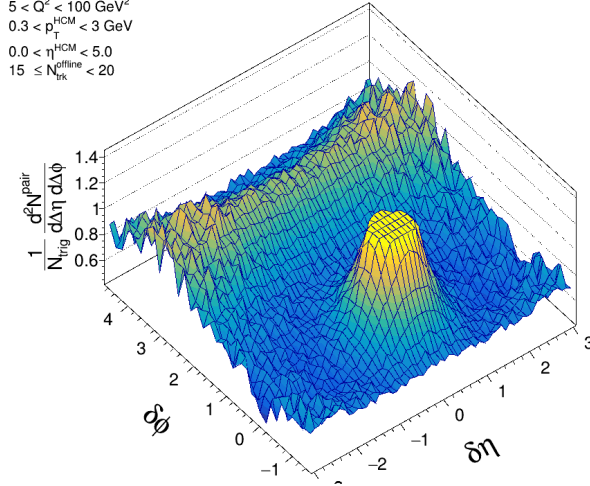
MC DJANGO DIS ( HCM frame )

$$\begin{aligned}
 &5 < Q^2 < 100 \text{ GeV}^2 \\
 &0.3 < p_T^{\text{HCM}} < 3 \text{ GeV} \\
 &0.0 < \eta^{\text{HCM}} < 5.0 \\
 &2 \leq N_{\text{trk}}^{\text{offline}} < 4
 \end{aligned}$$



MC RAPGAP DIS ( HCM frame )

$$\begin{aligned}
 &5 < Q^2 < 100 \text{ GeV}^2 \\
 &0.3 < p_T^{\text{HCM}} < 3 \text{ GeV} \\
 &0.0 < \eta^{\text{HCM}} < 5.0 \\
 &15 \leq N_{\text{trk}}^{\text{offline}} < 20
 \end{aligned}$$



MC RAPGAP DIS ( HCM frame )

$$\begin{aligned}
 &5 < Q^2 < 100 \text{ GeV}^2 \\
 &0.3 < p_T^{\text{HCM}} < 3 \text{ GeV} \\
 &0.0 < \eta^{\text{HCM}} < 5.0 \\
 &2 \leq N_{\text{trk}}^{\text{offline}} < 4
 \end{aligned}$$

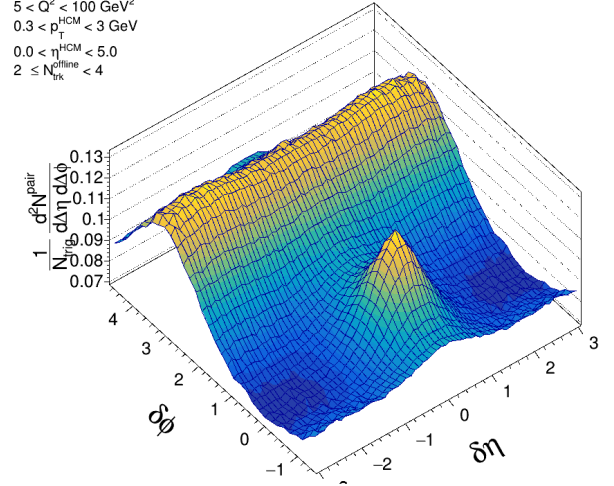


FIG. 16: 2PCs of MC simulations. Both of the MCs can well describe the 2PCs in ep H1 DIS in all multiplicities.

The  $V_{n,n}$  can be extracted from the long-range  $\Delta\eta$  region. After the non-flow removal procedures mentioned above, the subtracted  $V_{n,n}$  are shown versus multiplicity in FIG.18-19.

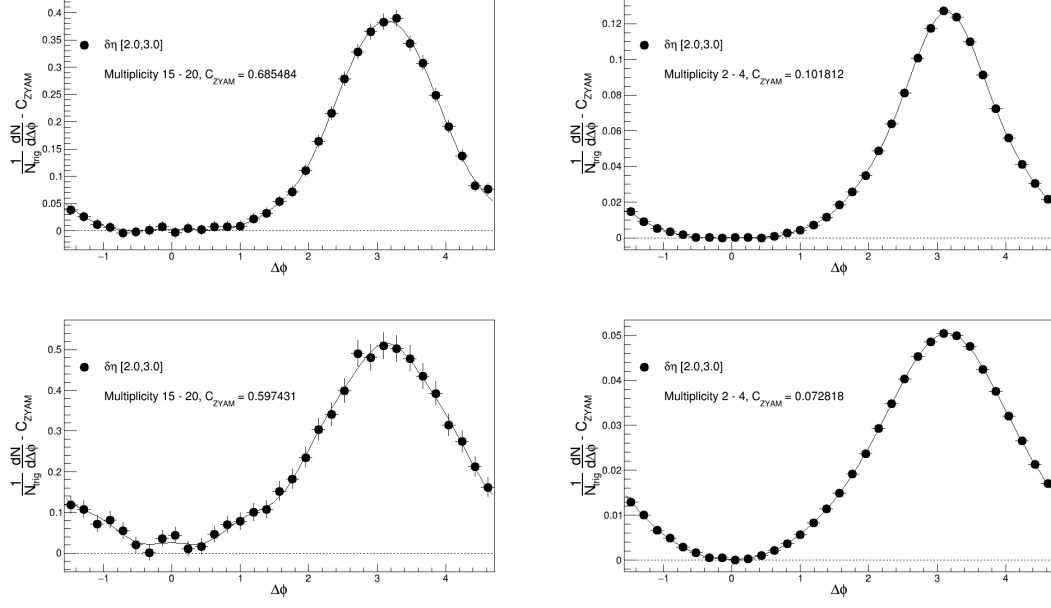


FIG. 17: The 1-D projection of the 2PC in ep DIS simultaions of MC DJANGO(up) and RAP-GAP(down).

Both of the MCs show that the peripheral subtraction over-subtracts the values of  $V_{n,n}$ , and the template fit results need further explanations.



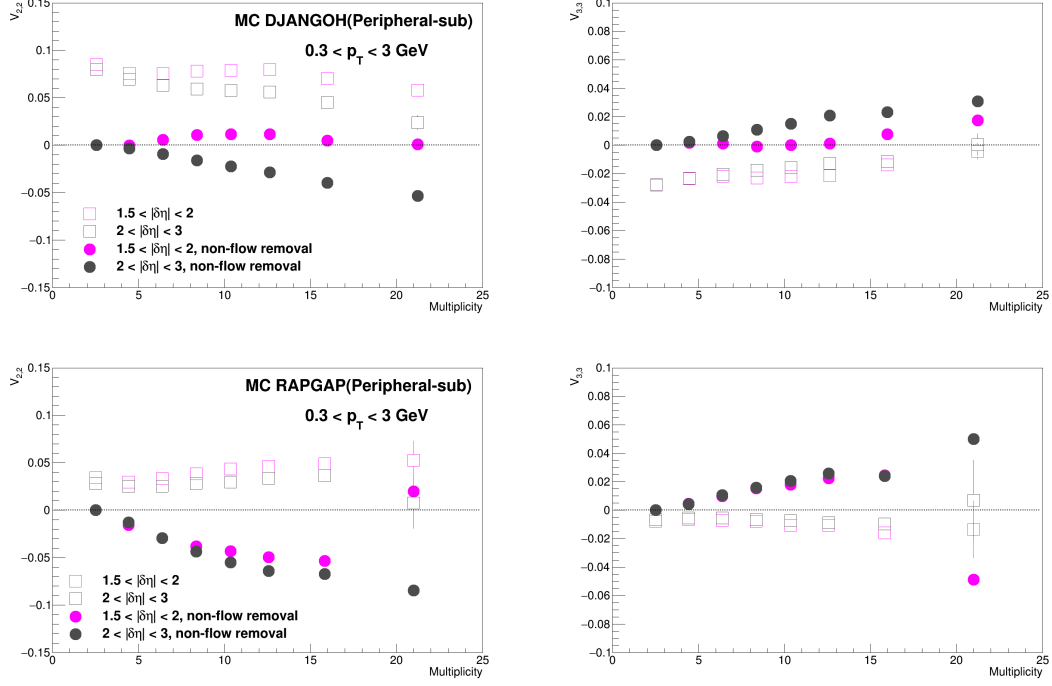


FIG. 18: Peripheral subtraction method in ep DIS MC DJANGO and MC RAPGAP, using multiplicity [2, 4] as the non-flow removal baseline.

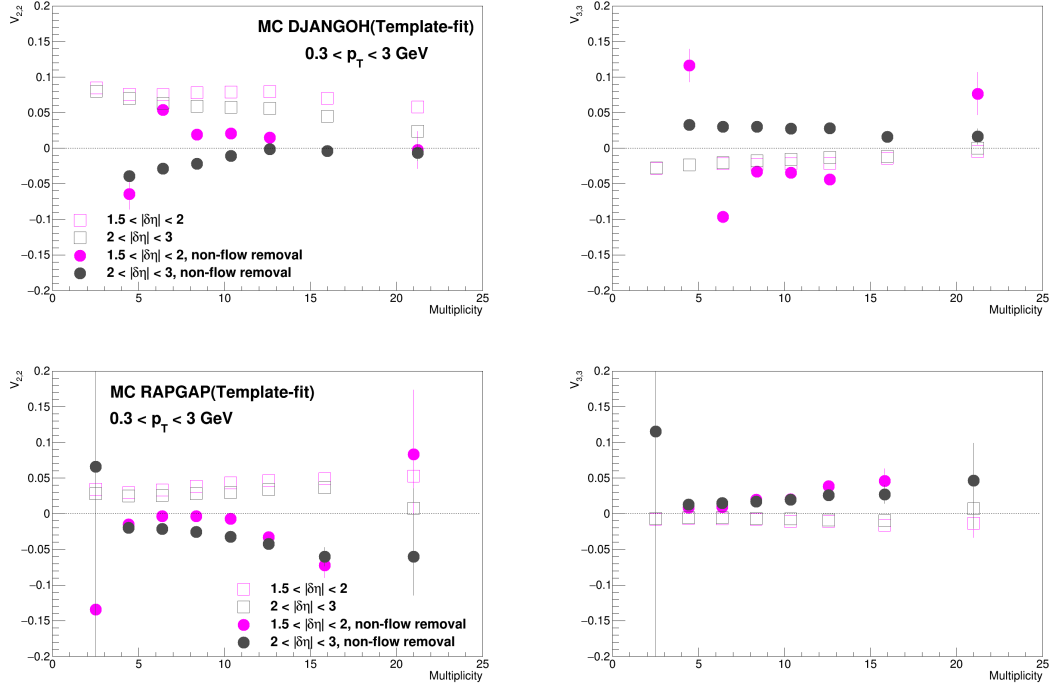


FIG. 19: Template fit method in ep DIS MC DJANGO and MC RAPGAP, using multiplicity [2, 4] as non-flow removal baseline.

## IV. RESULTS

### A. DIS Results

FIG.20. here compare the 2-D correlation functions between the low and high multiplicity, for charged particles with  $0.3 < p_T^{HCM} < 3$  GeV. For the low multiplicity situation ( $2 \leq N_{trk}^{offline} < 4$ ), the near-side feature in (0,0) originates from the short-range correlation dominated by the jet effects, and the away-side structure ranging in all eta direction is the results of the charged particles from the back-to-back jets. For the high multiplicity ( $15 \leq N_{trk}^{offline} < 20$ ), the structure is also similar. In all multiplicities, there's no obvious near-side ridge structure seen.

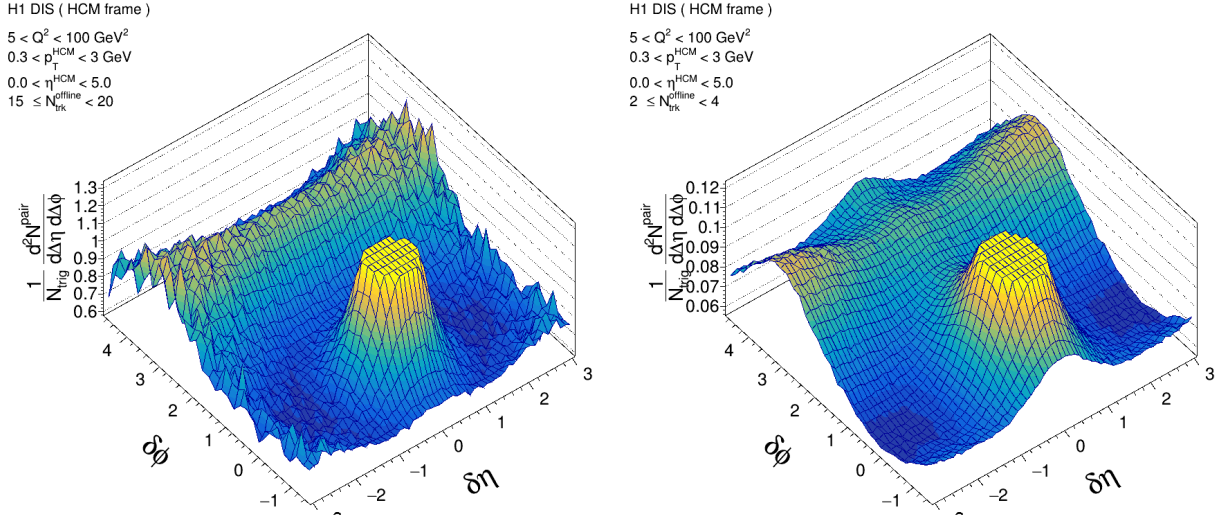


FIG. 20: 2PCs in high multiplicity events ( $15 \leq N_{trk}^{offline} < 20$ ), and in low multiplicity events ( $2 \leq N_{trk}^{offline} < 4$ ). The sharp near-side peaks from jet correlations has been truncated to better illustrate the structure outside that region.

In order to extract  $V_{n,n}$  information and to quantify the potential flow signal, the 1-D projections of the 2PC on the  $\Delta\phi$  direction and the non-flow removal procedure is required, which is listed in FIG.21.

In all multiplicity, there's no near-side ridge structure as a signal of collective flow. The  $V_{n,n}$  versus multiplicity results after non-flow removal are also listed in FIG.22.

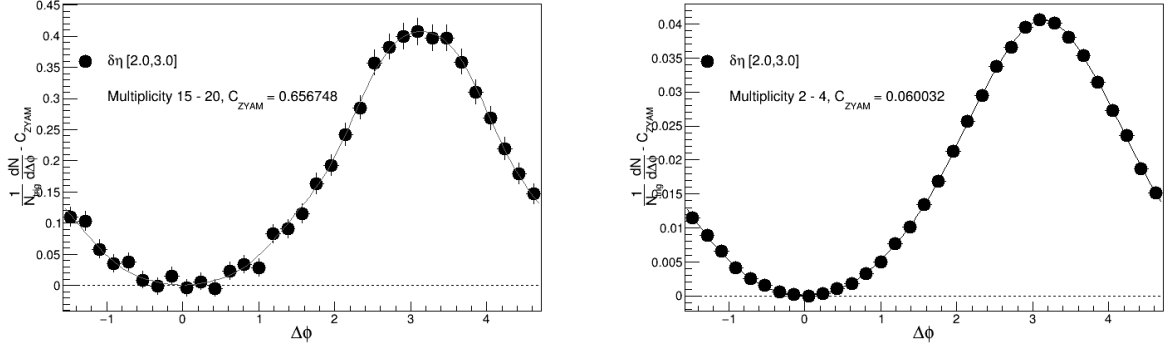


FIG. 21: 1-D projections of the 2PCs in ep H1 DIS processes.

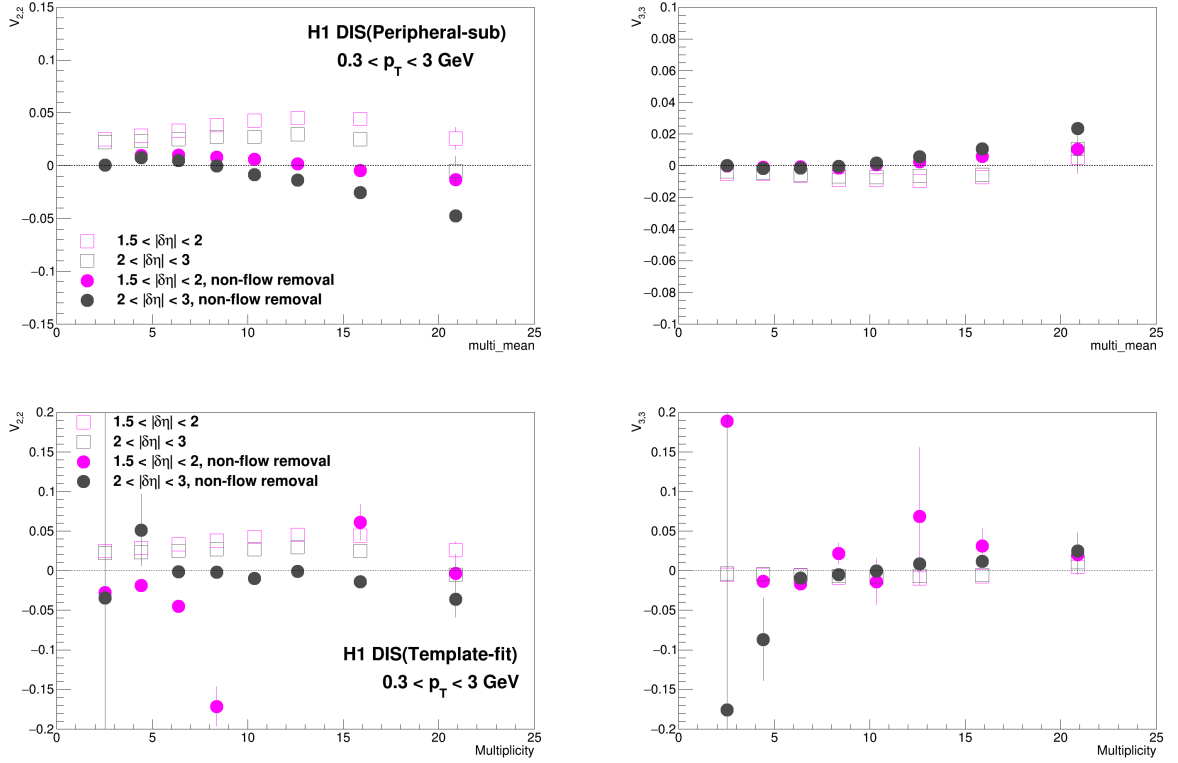


FIG. 22: The  $V_{2,2}$ ,  $V_{3,3}$  after two sorts of non-flow removal procedures in H1 ep DIS processes.

## B. Photoproduction Results

FIG.23 compare the 2-D correlation functions between the low and high multiplicity in ep photoproduction events, for charged particles with  $0.3 < p_T < 3$  GeV. There's no near-side ridge in any multiplicity. For the low multiplicity ( $2 \leq N_{trk}^{offline} < 4$ ), the near-side feature in (0,0) originates from the short-range correlation dominated by the jet effects, and the

away-side structure ranging in all  $\Delta\eta$  direction is the results of the charged particles from the back-to-back jets. For the high multiplicity ( $15 \leq N_{trk}^{offline} < 20$ ), the structure is also similar.

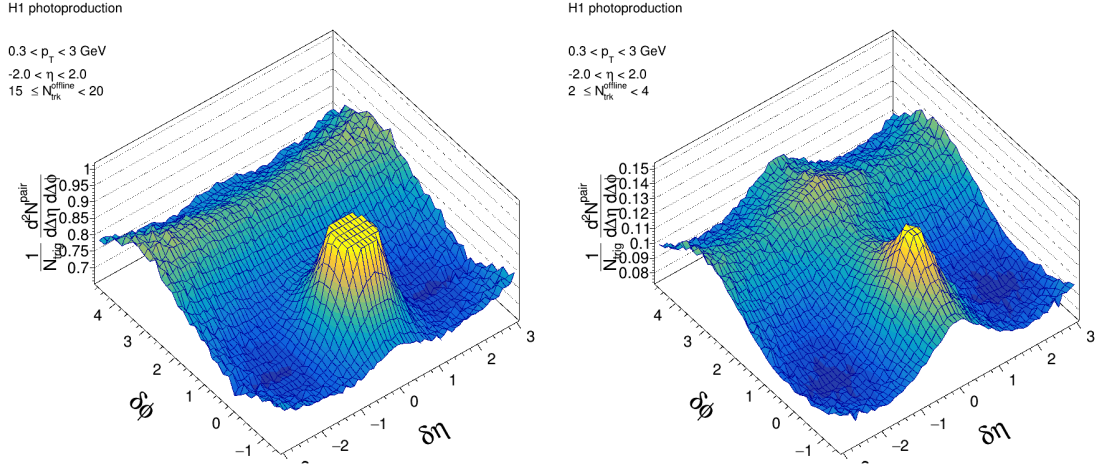


FIG. 23: 2PCs in high multiplicity events ( $15 \leq N_{trk}^{offline} < 20$ ), and in low multiplicity events ( $2 \leq N_{trk}^{offline} < 4$ ). The sharp near-side peaks from jet correlations has been truncated to better illustrate the structure outside that region.

To get quantative measurements, the 1-D projections of the 2PC and  $V_{n,n}$  without non-flow are needed, which are shown in FIG.24-25.

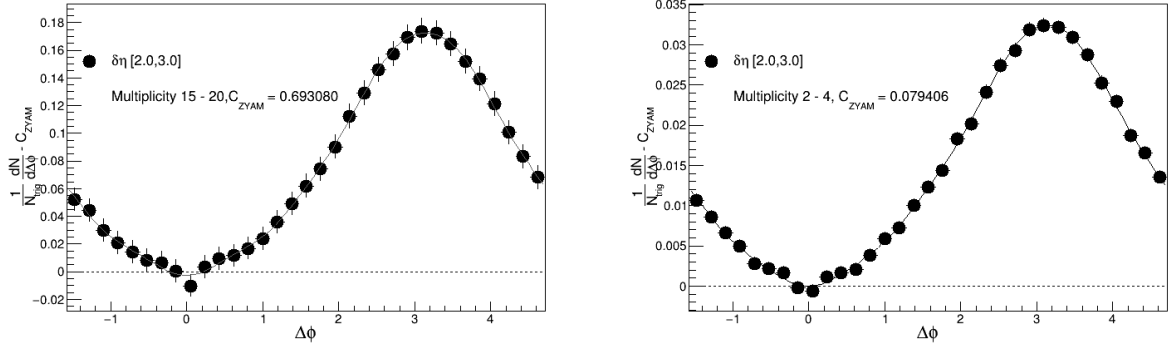


FIG. 24: 1-D projections of the 2PCs in ep H1 photoproduction processes.

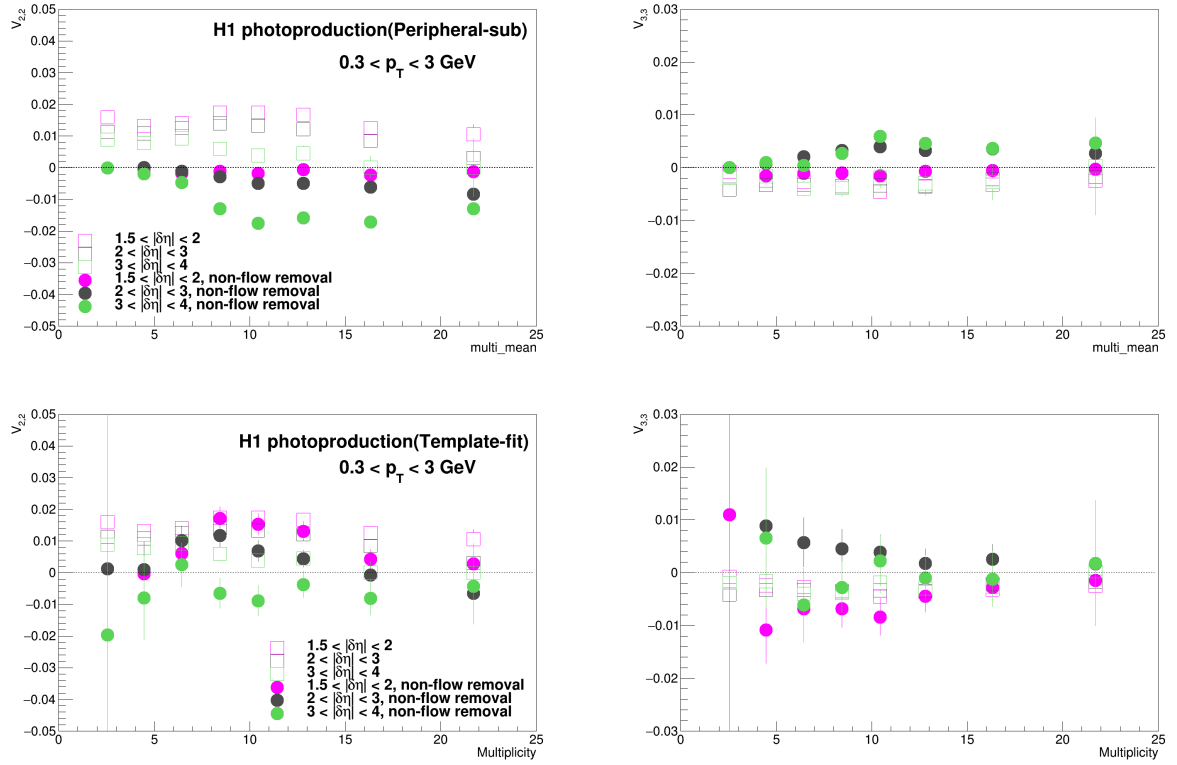


FIG. 25: The  $V_{2,2}$ ,  $V_{3,3}$  after non-flow removal procedures.

## V. CROSS CHECKS

Several cross checks on this analysis are documented here. To ensure the performance of the non-flow removal procedure, two-particle correlation functions within DIS and photoproduction selections should be weighted considering the event-by-event different centre-of-mass energy in ep collisions, as well as some modifications along current multiplicity divisions. It

is natural to keep subtracted multiplicity region(usually peripheral) with higher multiplicity ones have similar detector acceptances and non-flow fractions, and the detailed weighting procedures are described as follows.

The weighting processes are also applied in MC simulations of the DIS in ep collisions, within the properties  $Q^2$ ,  $y$  and  $p_T$ .

## A. Weighting in DIS

### 1. 2-D $Q^2$ and $y$ dependence on multiplicity

The centre-of-mass energies in photon and proton interactions would be affected by the random photon energy, and vary in large ranges. The changing collision energy induces different boost on detector acceptances in HCM frame, which requires that event level information should be weighted into same collision energy to ensure acceptances equivalent.

In this DIS analysis, a 2-D  $Q^2$  and  $y$  distribution is used to ensure these. As the statistics limited in multiplicity bins, a bin-by-bin ratio based on the 2-D functions from the original to highest multiplicity is not feasible. An alternative is to modify the peripheral one to higher multiplicity bins, which can provide non-flow informations directly. 1-D projections of the 2-D  $Q^2$  and  $y$  distributions are shown in FIG.26-27.

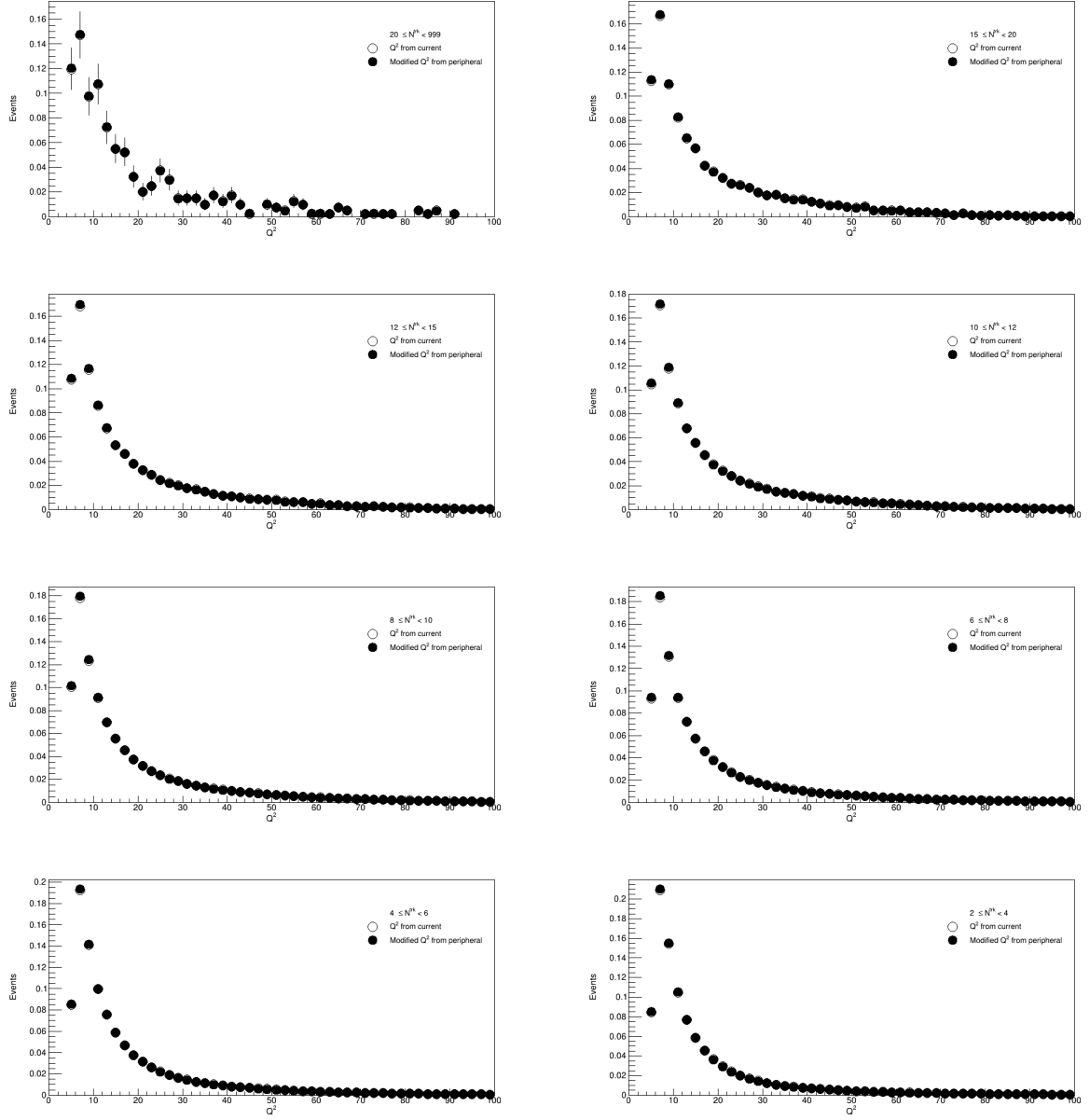


FIG. 26: The distributions of  $Q^2$  in weighted peripheral multiplicity(solid) and in original multiplicity(hollow) in  $0.3 < p_T^{HCM} < 3.0$  GeV,  $0.0 < \eta^{HCM} < 5.0$  ep DIS data. The bias is negligible.

## 2. $p_T$ dependence on multiplicity

The geometry shape basis of the non-flow removal procedure relies on the similar non-flow fractions in total correlations, which can be reflected by  $p_T$  values. Achieving same  $p_T$  distributions between the subtracting and subtracted multiplicity bins is the aim of this weighting. And the comparisons are shown in FIG.28.

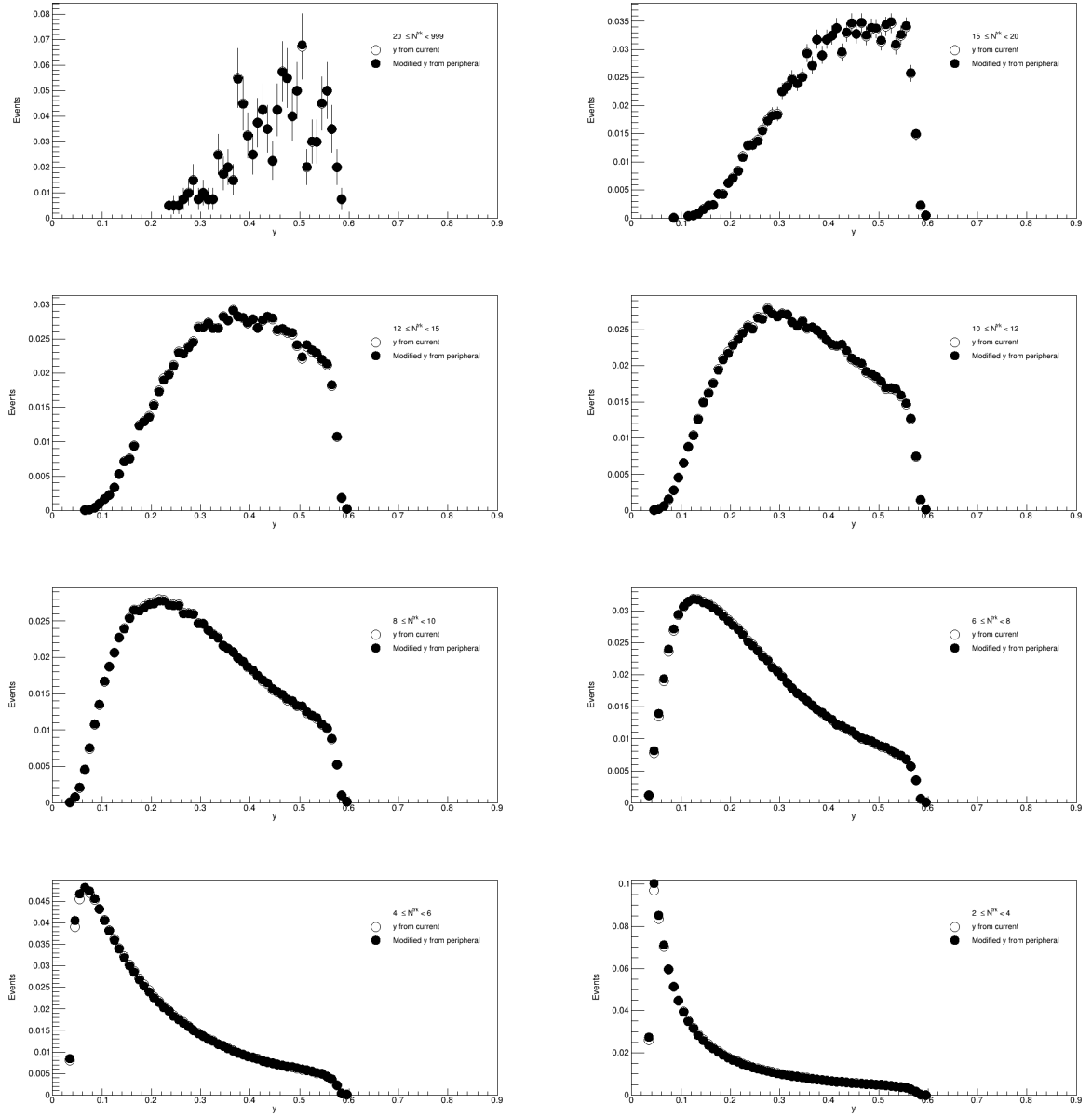


FIG. 27: The distributions of  $y$  in weighted peripheral multiplicity(solid) and in original multiplicity(hollow) in  $0.3 < p_T^{HCM} < 3.0$  GeV,  $0.0 < \eta^{HCM} < 5.0$  ep DIS data. The bias is negligible.

## B. Weighting in photoproductions

### 1. Centre-of-mass energy dependence on multiplicity

In photoproduction process, the centre-of-mass energy is calculated using the hadronic final state information. The weighting is aimed for this and listed in FIG.29.



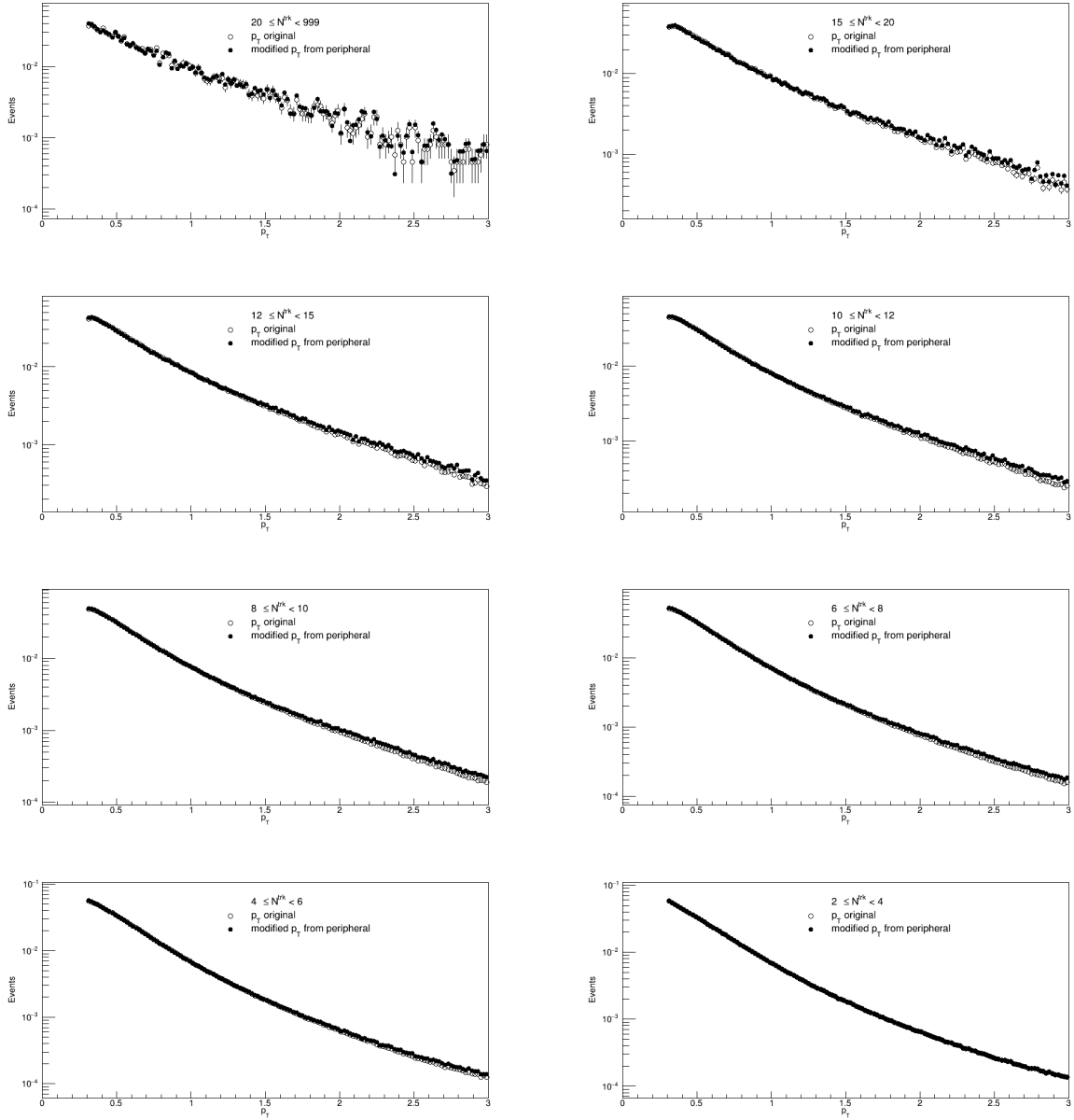


FIG. 28: The distributions of  $p_T$  in weighted peripheral multiplicity(solid) and in original multiplicity(hollow) in  $0.3 < p_T < 3.0$  GeV,  $-1.6 < \eta < 1.6$  ep DIS data. The bias is negligible.

## 2. $p_T$ dependence on multiplicity

Similar to the DIS  $p_T$  weighting procedure. Achieving same  $p_T$  distributions between the subtracting and subtracted multiplicity bins is the aim of this weighting. The distribution plots in each multiplicity are shown in FIG.30.

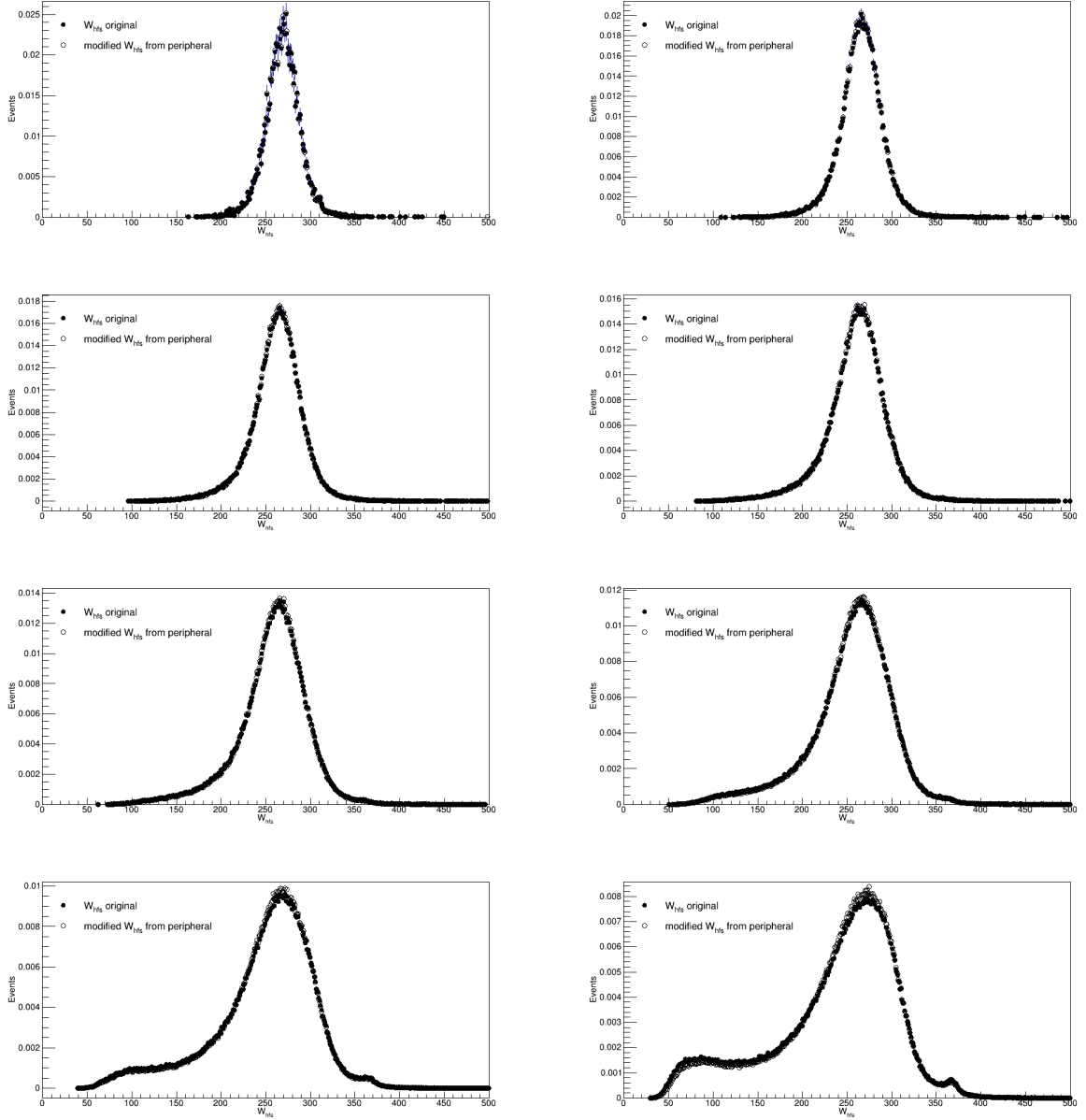


FIG. 29: The distributions of  $W_{hfs}$  in weighted peripheral multiplicity(hollow) and in original multiplicity(solid) in  $0.3 < p_T < 3.0$  GeV,  $-2.0 < \eta < 2.0$  ep photoproduction data. The bias is negligible.

### C. Higher peripheral multiplicity results

Considering the transition of physics, higher peripheral multiplicity are employed to get better non-flow removal capacity. The former results show the situation with  $[2, 4]$  as peripheral multiplicity, and here higher bins  $[4, 6]$ ,  $[6, 8]$  are also used.

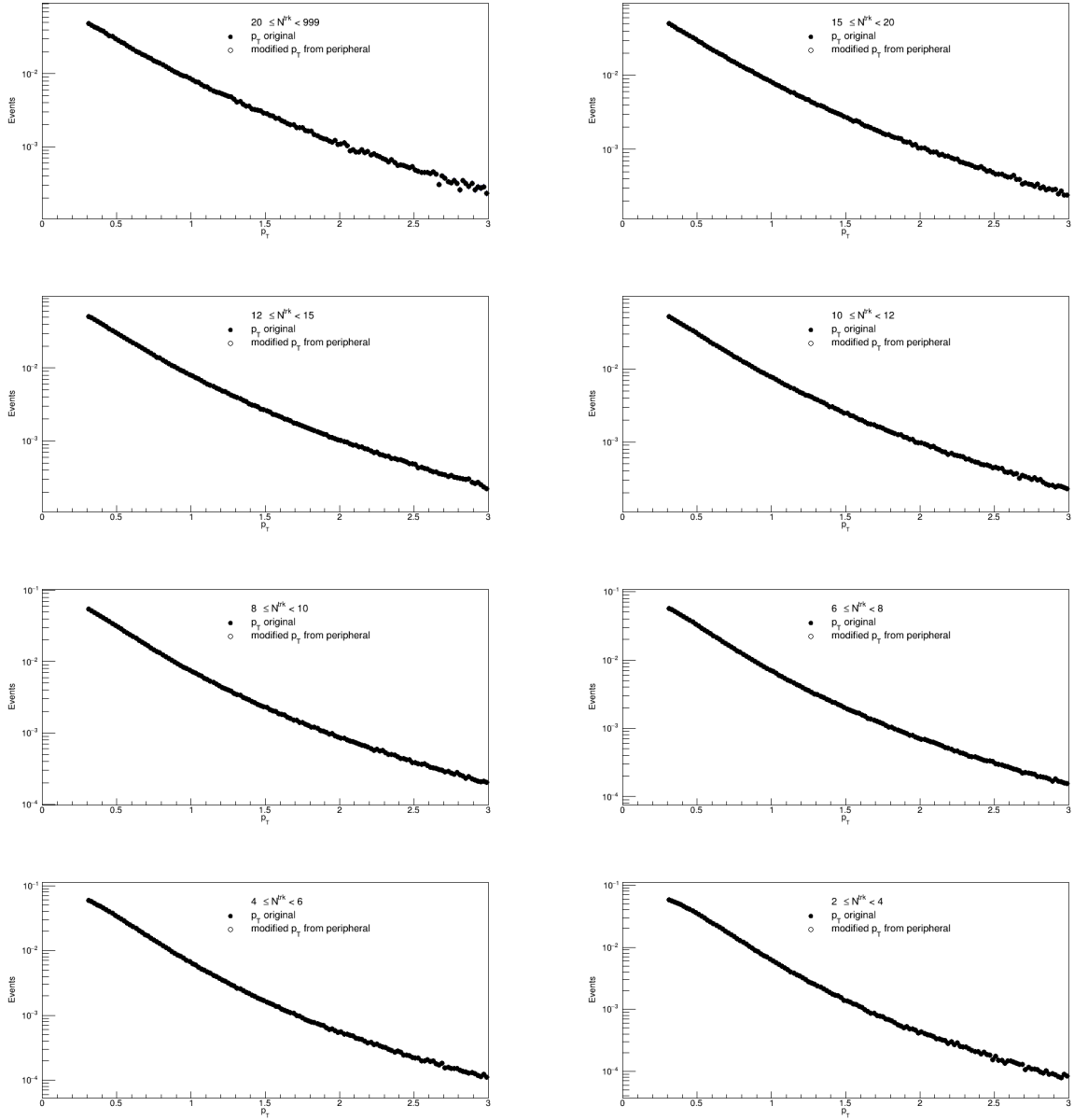


FIG. 30: The distributions of  $p_T$  in weighted peripheral multiplicity(hollow) and in original multiplicity(solid) in  $0.3 < p_T < 3.0$  GeV,  $-2.0 < \eta < 2.0$  ep photoproduction data. The bias is negligible.

### 1. Higher peripheral multiplicity results in MCs

The FIG.31-34 shows how  $V_{n,n}$  versus multiplicity changes within the difference of peripheral multiplicity selections in MCs.

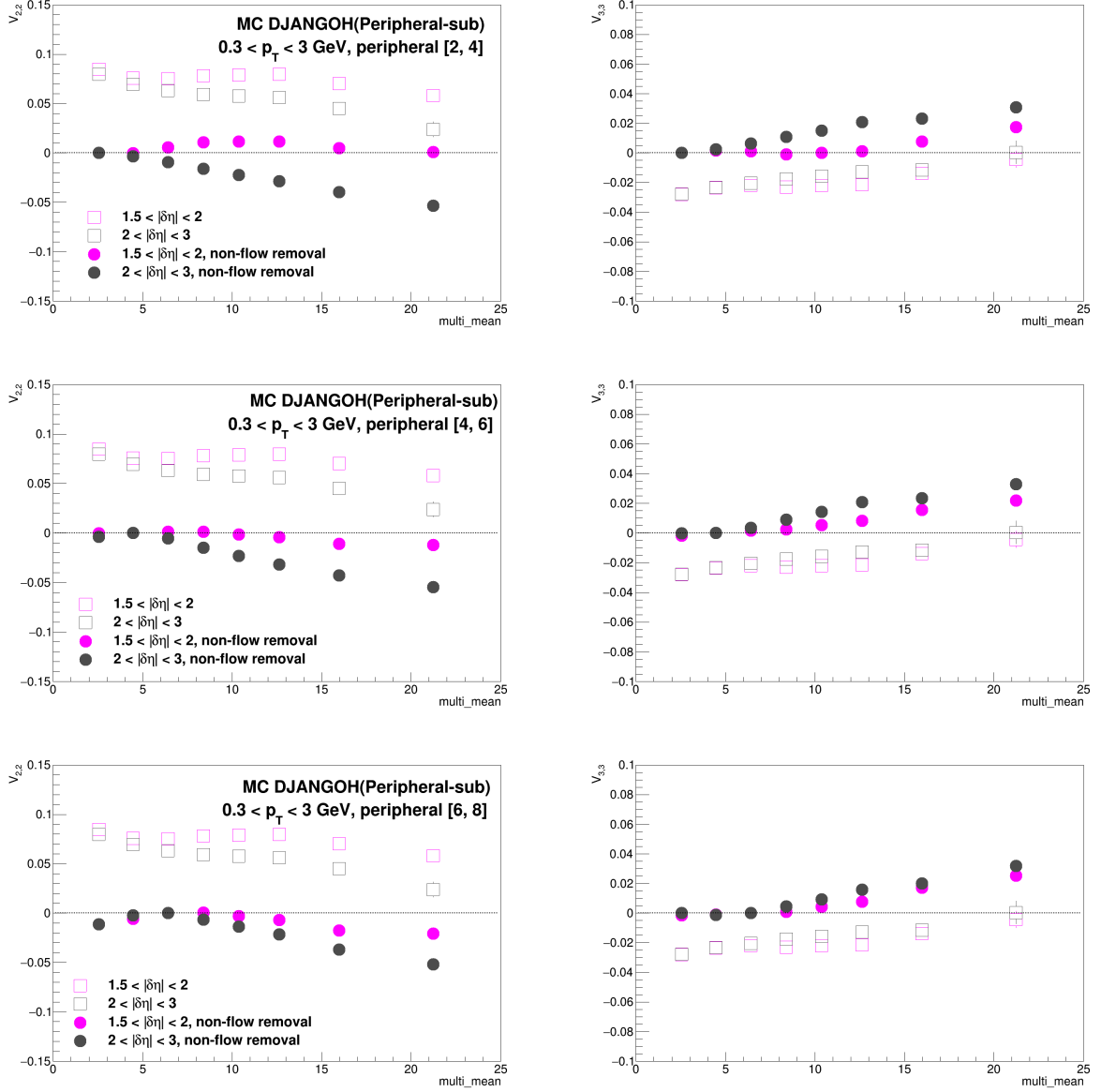


FIG. 31: After peripheral subtraction removal,  $V_{n,n}$  vs multiplicity varies with the changes in peripheral multiplicity in MC DJANGO simulations of DIS.

## 2. Higher peripheral multiplicity results in H1 data

The FIG.35-38 shows how  $V_{n,n}$  versus multiplicity changes within the difference of peripheral multiplicity selections in H1 data.

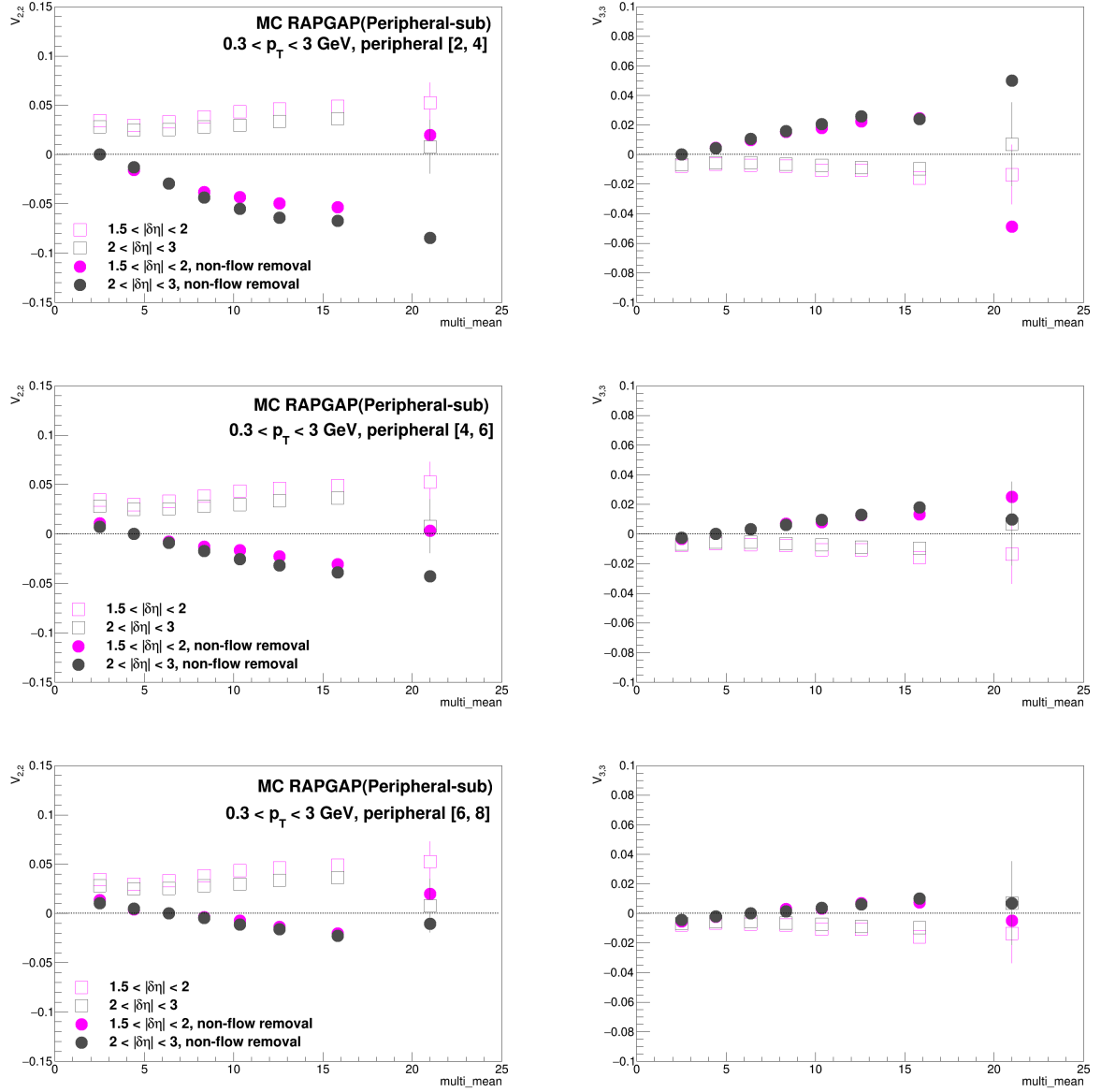


FIG. 32: After peripheral subtraction removal,  $V_{n,n}$  vs multiplicity varies with the changes in peripheral multiplicity in MC RAPGAP simultaitons of DIS.

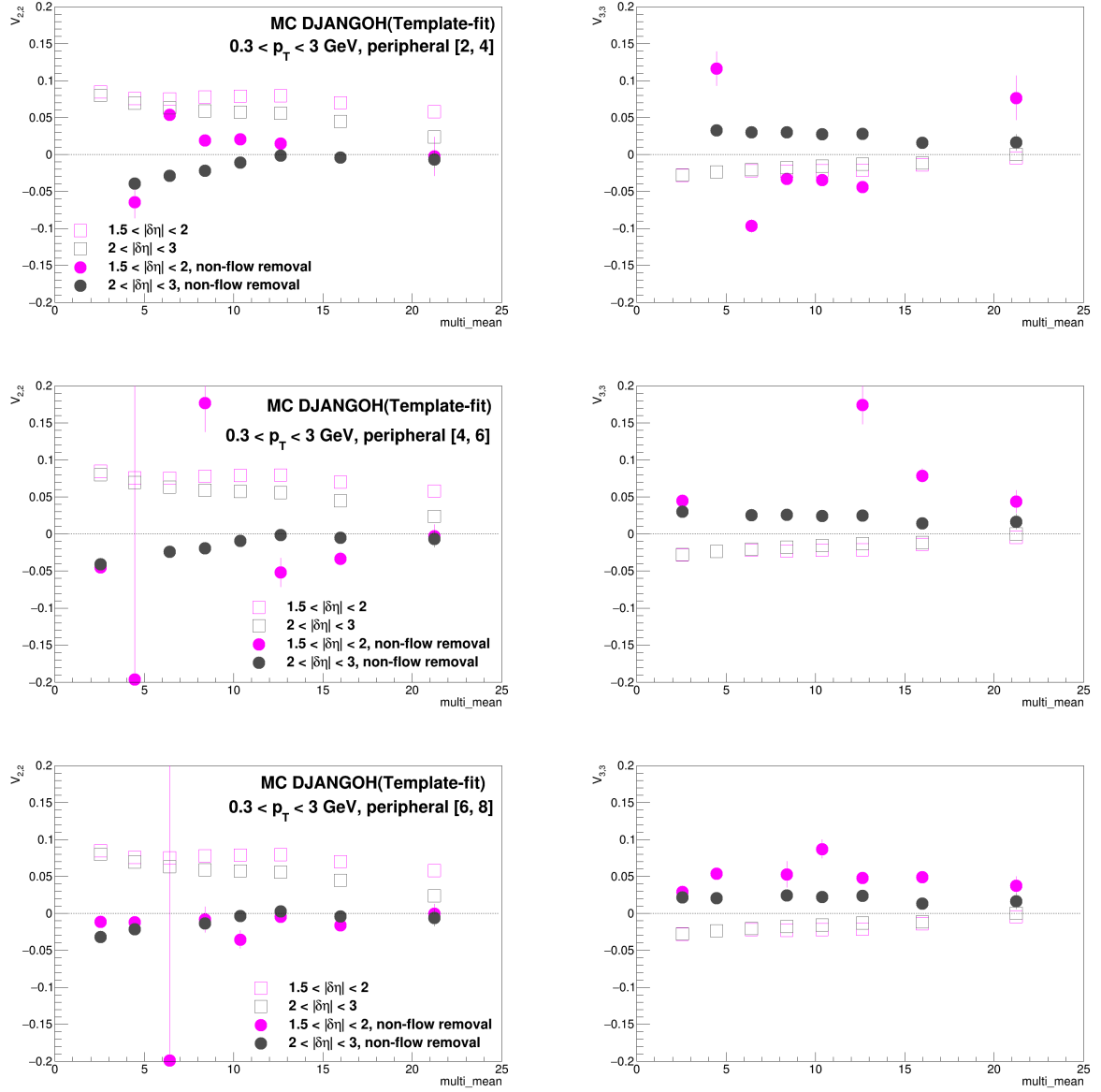


FIG. 33: After template fit removal,  $V_{n,n}$  vs multiplicity varies with the changes in peripheral multiplicity in MC DJANGO simulations of DIS.

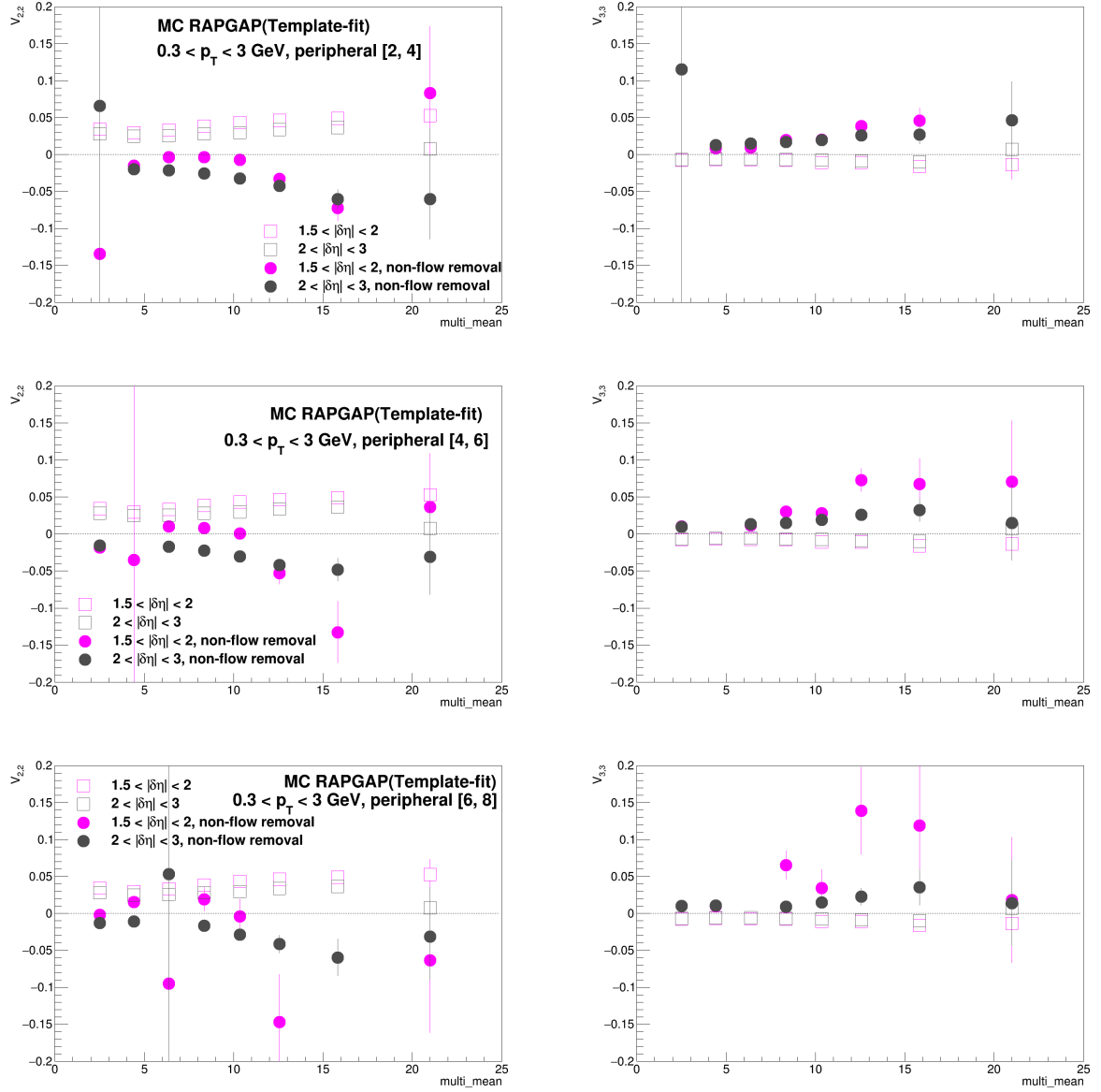


FIG. 34: After template fit removal,  $V_{n,n}$  vs multiplicity varies with the changes in peripheral multiplicity in MC RAPGAP simulations of DIS.

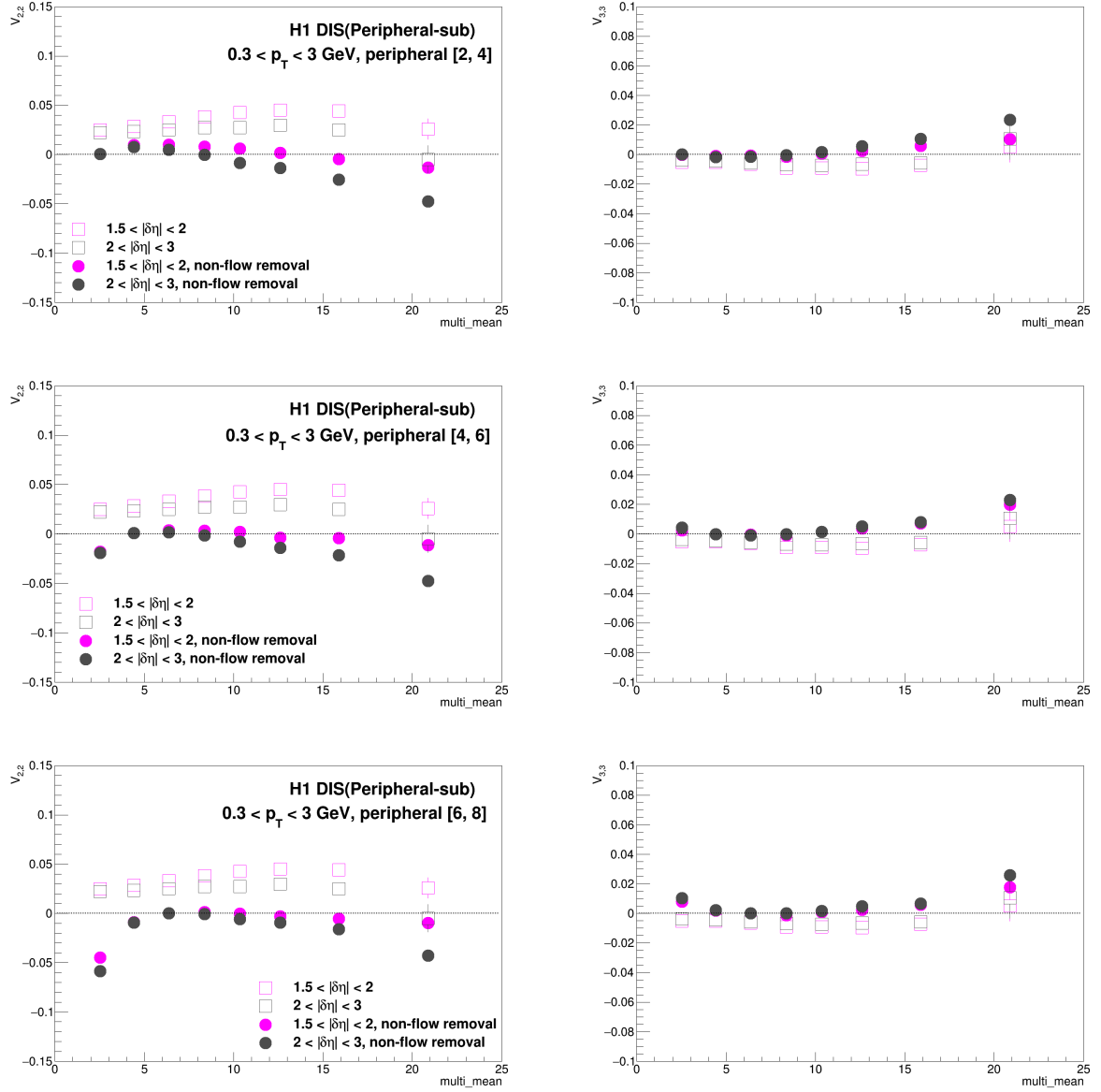


FIG. 35: After peripheral subtraction removal,  $V_{n,n}$  vs multiplicity varies with the changes in peripheral multiplicity in H1 DIS selections.



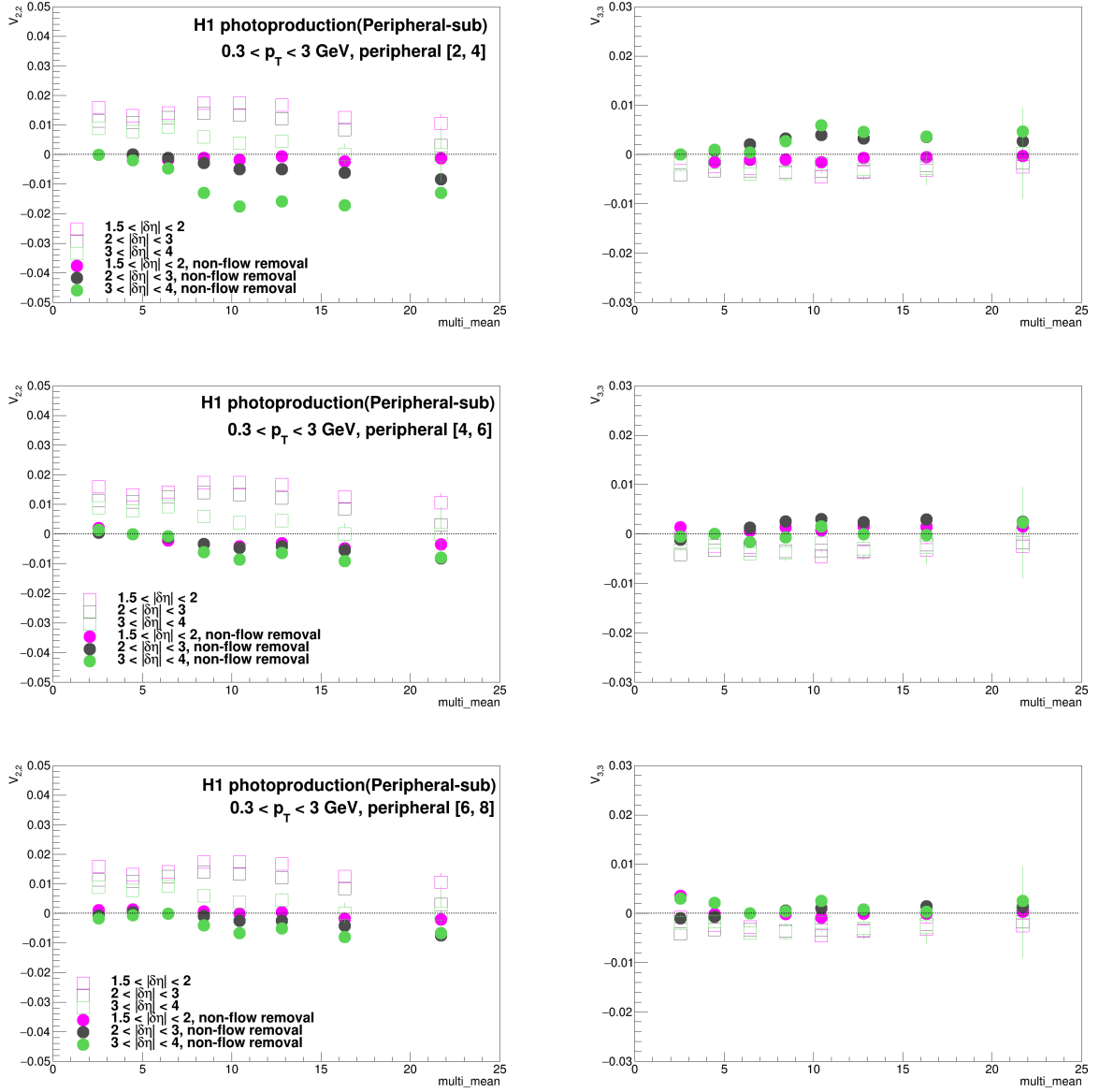


FIG. 36: After peripheral subtraction removal,  $V_{n,n}$  vs multiplicity varies with the changes in peripheral multiplicity in H1 photoproduction selections.

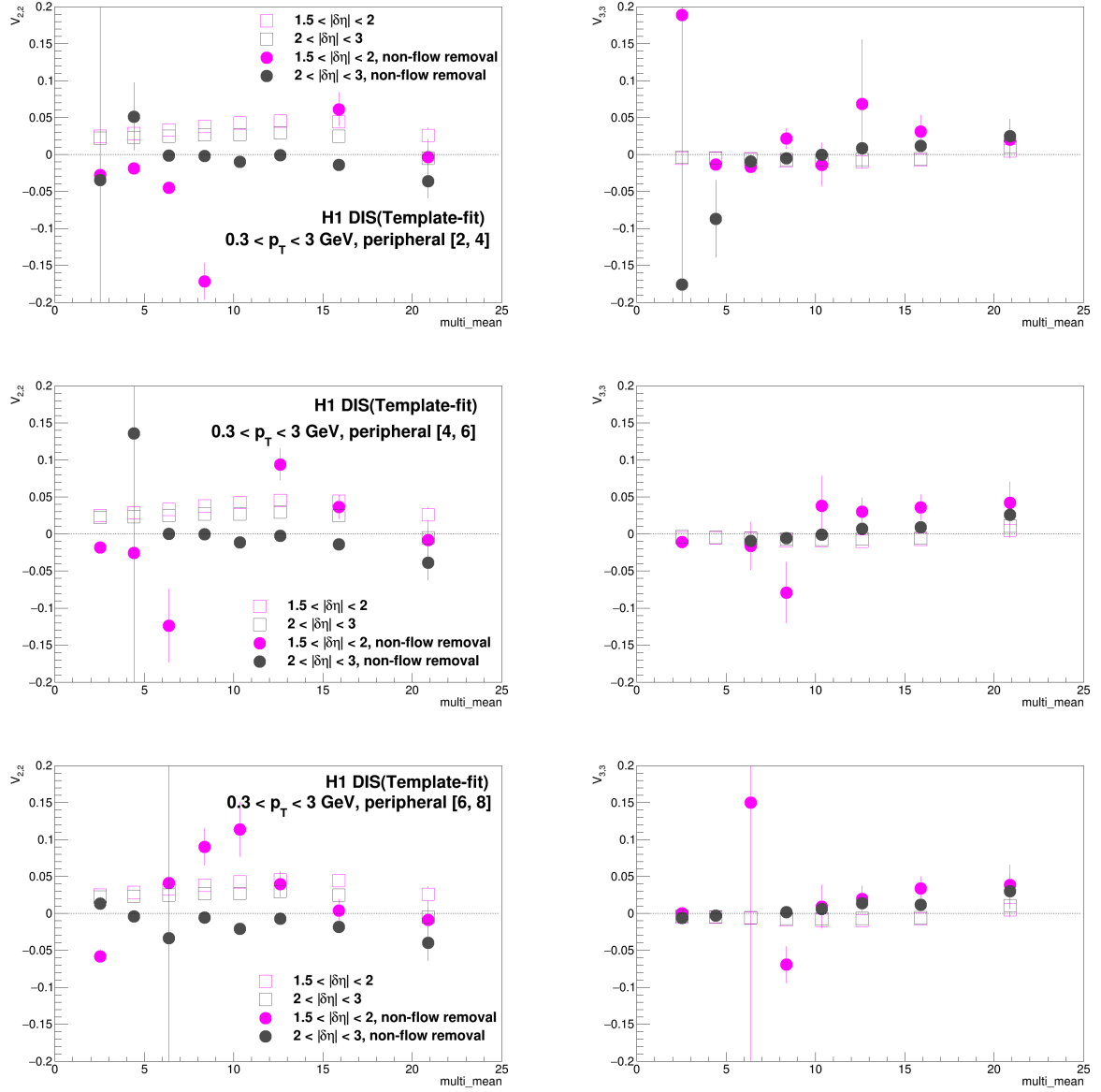


FIG. 37: After template fit removal,  $V_{n,n}$  vs multiplicity varies with the changes in peripheral multiplicity in H1 DIS selections.

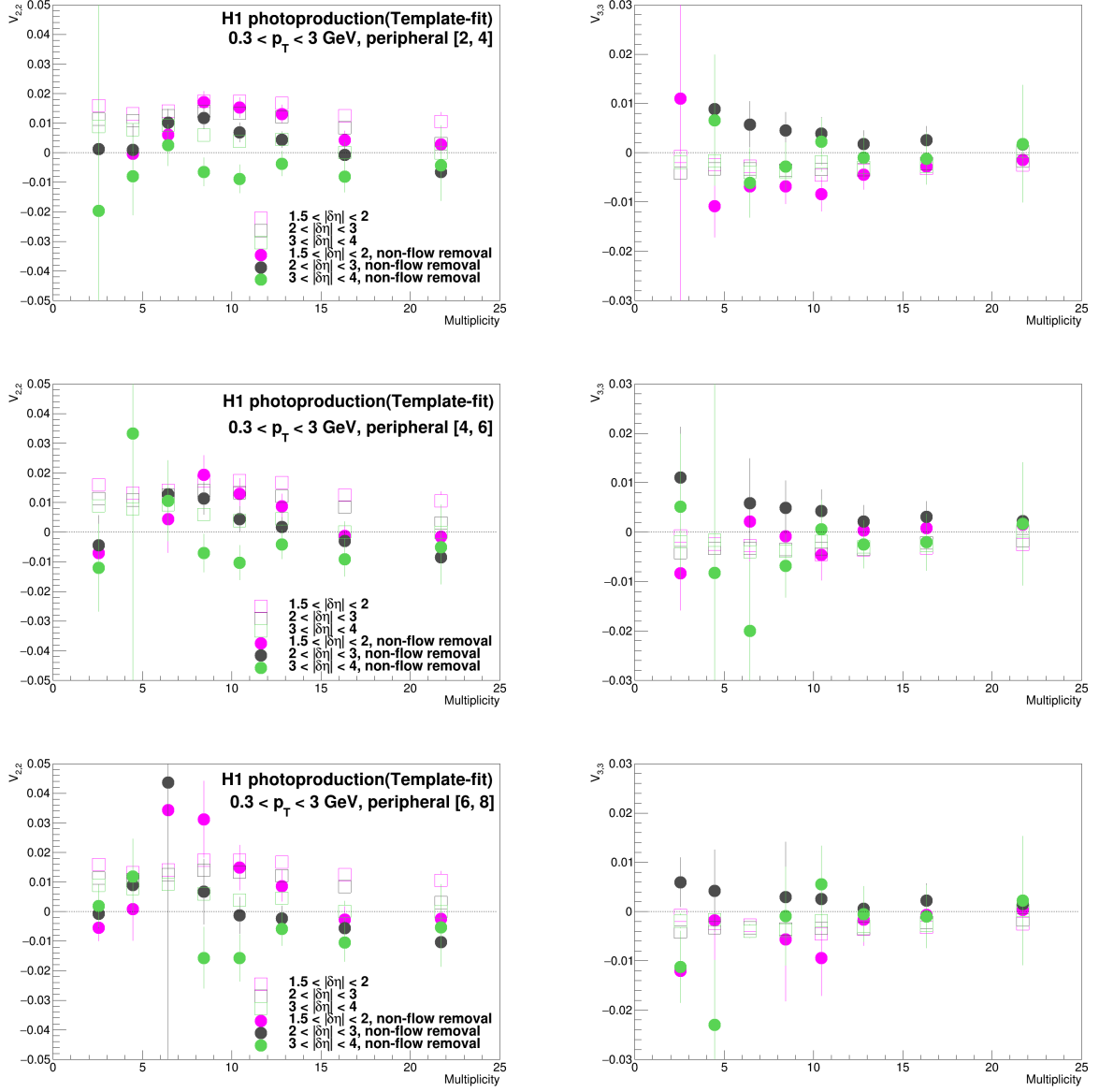


FIG. 38: After template fit removal,  $V_{n,n}$  vs multiplicity varies with the changes in peripheral multiplicity in H1 photoproduction selections.

## VI. SUMMARY

to be done.

- 
- [1] C. Alexa *et al.* [H1], Eur. Phys. J. C **73**, no.4, 2406 (2013) doi:10.1140/epjc/s10052-013-2406-x [arXiv:1302.1321 [hep-ex]].